

A deep radius valley revealed by *Kepler* short cadence observations

Cynthia S. K. Ho^{*} and Vincent Van Eylen

Mullard Space Science Laboratory, University College London, Dorking RH5 6NT, UK

Accepted 2022 December 19. Received 2022 December 2; in original form 2022 October 17

ABSTRACT

The characteristics of the radius valley, i.e., an observed lack of planets between 1.5–2 Earth radii at periods shorter than about 100 days, provide insights into the formation and evolution of close-in planets. We present a novel view of the radius valley by refitting the transits of 431 planets using *Kepler* 1-minute short cadence observations, the vast majority of which have not been previously analysed in this way. In some cases, the updated planetary parameters differ significantly from previous studies, resulting in a deeper radius valley than previously observed. This suggests that planets are likely to have a more homogeneous core composition at formation. Furthermore, using support-vector machines, we find that the radius valley location strongly depends on orbital period and stellar mass and weakly depends on stellar age, with $\partial \log(R_{p,\text{valley}})/\partial \log P = -0.096^{+0.023}_{-0.027}$, $\partial \log(R_{p,\text{valley}})/\partial \log M_{\star} = 0.231^{+0.053}_{-0.064}$, and $\partial \log(R_{p,\text{valley}})/\partial \log(\text{age}) = 0.033^{+0.017}_{-0.025}$. These findings favour thermally-driven mass loss models such as photoevaporation and core-powered mass loss, with a slight preference for the latter scenario. Finally, this work highlights the value of transit observations with short photometric cadence to precisely determine planet radii, and we provide an updated list of precisely and homogeneously determined parameters for the planets in our sample.

Key words: planets and satellites: composition – planets and satellites: formation – planets and satellites: fundamental parameters

1 INTRODUCTION

The ‘radius valley’, also known as the ‘radius gap’, is the relative paucity of planets with sizes between about 1.5 and 2 Earth radii at orbital periods less than about 100 days. This phenomenon has been predicted theoretically due to the heavy radiation these close-in planets receive from their host star (e.g. [Owen & Wu 2013](#); [Lopez & Fortney 2013](#)) and was subsequently seen observationally (e.g. [Fulton et al. 2017](#); [Van Eylen et al. 2018](#); [Fulton & Petigura 2018](#)). Several theories have been suggested to explain the physical origin of the radius valley. On one hand, thermally-driven mass loss scenarios have been proposed, which include photoevaporation (e.g. [Owen & Wu 2013](#); [Lopez & Fortney 2013](#); [Owen & Wu 2017](#)) and core-powered mass loss (e.g. [Ginzburg et al. 2018](#); [Gupta & Schlichting 2019, 2020](#)) models. In these scenarios, the valley separates planets that have lost their atmosphere from those that have retained it. Alternatively, late gas-poor formation, where planets below the valley have formed atmosphere-free, may also be able to explain the origin of the valley (e.g. [Lee et al. 2014](#); [Lee & Chiang 2016](#); [Lopez & Rice 2018](#); [Cloutier & Menou 2020](#)).

Observed characteristics of the radius valley can therefore reveal the properties of these close-in planets and their formation history. For example, in photoevaporation models, the location of the radius valley and its slope as a function of orbital period depend on the planetary composition and photoevaporation physics ([Owen & Wu 2017](#); [Mordasini 2020](#)). The valley’s location and relative emptiness can therefore be used to infer the composition of planets surrounding it and their relative homogeneity (e.g. [Van Eylen et al. 2018](#)). Planets

located inside the radius valley may have a different composition or could be undergoing the final stages of atmospheric loss by thermally-driven mechanisms and hence may be important targets for further studies (e.g. [Owen & Wu 2017](#); [Gupta & Schlichting 2019](#); [Petigura 2020](#)). The valley’s location as a function of orbital period can be used to distinguish between thermal mass-loss models, which exhibit a negative slope as a function of orbital period, and late gas-poor formation models which have the opposite slope (e.g. [Van Eylen et al. 2019](#); [Cloutier & Menou 2020](#); [Van Eylen et al. 2021](#)). Within thermal mass-loss models, photoevaporation and core-powered mass loss models predict a different dependence of the valley’s location on stellar mass and age (e.g. [Rogers et al. 2021](#)).

Observationally, these valley characteristics have been challenging to reliably ascertain. A deficit of planets with sizes around 1.5–2 Earth radii (R_{\oplus}) was first observed by [Fulton et al. \(2017\)](#) in a sample of 2025 planets, with stellar radii determined spectroscopically as part of the *California-Kepler* survey (CKS). These planets were about a factor of two rarer than planets both smaller and larger. Independently, [Van Eylen et al. \(2018\)](#) (V18 hereafter) analysed a subset of this sample (117 planets), incorporating higher-precision stellar parameters using asteroseismology and refitting transit light curves to achieve a median uncertainty on planet sizes of 3.3%. This study revealed the valley’s slope as a function of orbital period for the first time, and suggested the radius valley may be very deep or even entirely empty. The tension between the valley’s views of [Fulton et al. \(2017\)](#) and V18 was further exacerbated when the precision of stellar parameters of the former study were further improved by [Fulton & Petigura \(2018\)](#) (F18 hereafter). Despite improving stellar uncertainties from 11% to 3% by incorporating Gaia parallaxes, the valley remained partially filled in, with its depth largely unchanged.

* E-mail: sze.ho.20@ucl.ac.uk

Petigura (2020) investigated the discrepancy in the valley’s depth between V18 and F18 and concluded it is unlikely to be caused by differing sample sizes or differing values or uncertainties in stellar radii. The study argued that the 6.9% dispersion in planetary radii is instead primarily caused by a discrepancy in the ratio of planet to stellar radii (R_p/R_\star) determined from the transit fits. F18 used radius ratios from Mullally et al. (2015), which fitted *Kepler* 30-minute ‘long cadence’ observations, whereas V18 used *Kepler* 1-minute ‘short cadence’ observations, also used for orbital eccentricity determination and described in Van Eynen & Albrecht (2015) and Van Eynen et al. (2019).

Here, we seek to refit planet transits for the full subset of F18 for which short cadence observations are available. This increases the sample of planets relevant for the radius valley for which short cadence transit fits are used from 60 in V18 to 431 here. Furthermore, we will apply the methods to determine the valley’s location and slope used by V18, notably the use of support vector machines, to this larger sample, and we expand to other dimensions such as stellar mass and age.

In Section 2, we describe the sample and methodology used to analyse the radius valley. In Section 3, we present the results of this analysis, such as revised planetary sizes, the depth of the valley, and its dependence on parameters such as the orbital period and stellar mass and age. These findings are compared to other observational studies and theoretical models in Section 4. Finally, we provide conclusions in Section 5.

2 METHODS

2.1 Sample selection

We use the sample of planets for which stellar parameters are available from F18 as a starting point. To focus on the radius valley, we limit the sample to planets with radii $1 \leq R_p/R_\oplus \leq 4$ and orbital periods $1 \leq P/\text{days} \leq 100$, resulting in a sample of 1272 planets (for comparison, applying the same period and radius cuts to the sample studied by V18 leaves 74 planets). As *Kepler* 1-minute short cadence observations may yield superior precision (Petigura 2020), we further limit our sample to those planets for which at least 6 months of *Kepler* short cadence data are available.

To avoid issues with transit fitting related to transit timing variations (TTVs), we also remove planets with known TTVs based on the catalogue by Holczer et al. (2016). We further exclude KOI-1576.03, as we find that the short cadence data suggested an orbital period different to the one recorded in the archive. Furthermore, we exclude any planets that are classified as potential false positives in Petigura et al. (2017). The results in a total sample size of 431 planets, 60 of which have parameters previously analysed by V18 and 371 which have not (a further 14 planets in V18 have TTVs and are not reanalysed here).

2.2 Data reduction

The 1-minute *Kepler* short cadence Pre-search Data Conditioning SAP (PDCSAP, Stumpe et al. 2012; Smith et al. 2012) light curves of these targets are downloaded from the NASA Mikulski Archive for Space Telescopes (MAST) database using the `lightkurve` package (Lightkurve Collaboration et al. 2018), which incorporates `astroquery` (Ginsburg et al. 2019) and `astropy` (Astropy Collaboration et al. 2013, 2018) dependencies. We only retain data within 0.2 days before the estimated ingress and after the estimated egress of the transits of the planets of interest, using the transit durations and

mid-times in Mullally et al. (2015) as the expected transit locations. For multi-planet systems, we only retain transits of planets that are within our sample. We remove data outliers that lie beyond 6σ from the median after masking the transits. We then flatten the transits by dividing the data points with the slope obtained by performing linear regression on the data points immediately before ingress and after egress, to remove long-term systematic trends present in the transits. We then again remove data outliers with $\sigma = 5$ to further clean the data.

2.3 Stellar multiplicity

Around 46% of solar-type stars have at least one stellar companion (Raghavan et al. 2010). When a planet orbits a single star, the transit depth δ is approximately given by

$$\delta = \frac{\Delta F}{F_{\text{tot}}} \approx \frac{R_p^2}{R_\star^2} \quad (1)$$

where F_{tot} is the total stellar flux, ΔF is the change in stellar flux, and R_p and R_\star are the planetary and stellar radius respectively. However, in a multi-stellar system, the total flux is the sum of fluxes of all stars in the system, but the change in flux during transit is only relative to the star(s) which the planet transits (Furlan et al. 2017). Therefore it is important to take into account the effect of nearby stars on the light curve flux.

Furlan et al. (2017) compiled a catalogue of *Kepler* Objects of Interest (KOI) observations with adaptive optics, speckle interferometry, lucky imaging, and imaging from space with the Hubble Space Telescope. The typical point spread function (PSF) widths and sensitivities (Δm) are different for every observation method, target and bandpass, hence whether stellar companions are detected is dependent on the above factors. For example, Furlan et al. (2017) were able to detect a median $\Delta m \sim 8\text{mag}$ with Keck in the *K* band at a separation of $\sim 0.5''$, but only at $\sim 2.5''$ at Lick in the *J* or *H* bands. About 30% of KOIs observed in Furlan et al. (2017) have at least one companion detected within $4''$ (Furlan et al. 2017), and given a mean distance of 616pc for the 431 planets in our sample computed from distances reported in Mathur et al. (2017), corresponds to $\sim 2464\text{AU}$.

Here, we adopt the ‘radius correction factor’ (RCF), given in Furlan et al. (2017) as

$$\text{RCF} = \frac{R_{p,\text{corr}}}{R_{p,\text{uncorr}}} \quad (2)$$

and multiply the normalised *Kepler* light curve fluxes by RCF^2 , and subtract $(\text{RCF}^2 - 1)$ to re-normalise, to obtain the corrected light curve reflecting the transit of one planet orbiting around one star. 137 of the 431 planets in our sample (32%) have RCF measurements from Furlan et al. (2017).

2.4 Transit fitting

We use the `exoplanet` package (Foreman-Mackey et al. 2021) to generate a transit light curve model with quadratic stellar limb darkening, and then run a Hamiltonian Monte Carlo (HMC) algorithm implemented in `PyMC3` (Salvatier et al. 2016) to perform fitting and determine orbital parameter posteriors. We also implement a Gaussian Process (GP) model (Rasmussen & Williams 2006) to account for correlated noise in the light curves. However, for Kepler-65 and Kepler-21 A, we do not fit for a GP model due to convergence constraints. The parameters fitted for each planet are orbital period (P), transit mid-time (t_0), ratio between planetary and stellar radii

(R_p/R_\star), impact parameter (b), eccentricity (e), argument of periastron (ω), and stellar density (ρ_\star). For each light curve, we further include two quadratic stellar limb darkening parameters (u_0 and u_1) for the host star, with bounds $0 < u_0, u_1 < 1$ and implemented with the Kipping (2013) reparameterisation in `exoplanet`, the transit jitter (σ_{LC}), and two parameters describing the GP contribution (σ_{gp} , ρ_{gp}).

We initialise the HMC chains by using values presented in the *Kepler* Q1-16 dataset (Mullally et al. 2015) for P , t_0 , R_p/R_\star , and b . We set the system to begin with near-circular orbits, with $e = 0.01$ and $\omega = 0.01$ rad. We take initial stellar densities from Fulton & Petigura (2018). We use the Exoplanet Characterization Toolkit (ExoCTK) (Bourque et al. 2021) to estimate the initial u_0 and u_1 , which takes the stellar temperature, surface gravity, and metallicity, which we use values from the *Kepler* Q1-16 dataset (Mullally et al. 2015), as inputs.

We apply Gaussian priors to P , t_0 , u_0 , u_1 , and ρ_\star , using the initial guesses as the mean, and $\sigma_P = 2 \times 10^{-5}$ days, $\sigma_{t_0} = 10^{-3}$ days, $\sigma_{u_i} = 0.2$, and the ρ_\star uncertainty from Fulton & Petigura (2018) if available, and Mullally et al. (2015) otherwise. A beta distribution prior according to Van Eylen et al. (2019) is placed on e , which is

$$\text{PDF}(e, \alpha, \beta) \propto e^\alpha (1 - e)^\beta \quad (3)$$

with $\alpha = 1.58$ and $\beta = 4.4$ for system with only one transiting planet, and $\alpha = 1.52$ and $\beta = 29$ for a multi-transiting-planet system.

3 RESULTS

3.1 Revised planet parameters

We report the updated orbital periods (P), planetary-to-stellar-radii ratio (R_p/R_\star), planetary radii (R_p), the number of transits in the fitted light curve (N_{tr}), and their uncertainties of the 431 planets fitted in this sample in Table 1. The full list of parameters are provided in Appendix A. We convert our R_p/R_\star to R_p using the updated stellar parameters available: values used in V18 from asteroseismology (i.e. taken from Huber et al. 2013; Silva Aguirre et al. 2015; Lundkvist et al. 2016) if the planets are included in the V18 samples, and F18 otherwise. Full homogeneity is lost by using stellar radii from two sources. To investigate the consequences of this, we compute the difference, δ_{R_p} , between the planetary radii obtained by converting R_p/R_\star to R_p using R_\star from F18 and V18, and found the mean δ , $\bar{\delta} = 0.03 \pm 0.11$, hence $\delta = 0$ (no difference) is well within 1σ , and we conclude that there is no substantial drawbacks of using multiple sources. This sample of 431 planets with updated parameters is plotted on the radius-orbital period plot as shown in Figure 1.

We present the typical uncertainties of R_p/R_\star and R_p of planets fitted in this work, compared with F18 and V18 in Table 2. For our newly fitted results, we find that R_p/R_\star has a mean uncertainty of 4.76%, and a median uncertainty of 3.44%. This is smaller when compared to the mean and median uncertainties of 8.73% and 4.07% respectively for the F18 sample. For R_p , we find a mean and median uncertainty of 6.09% and 4.70% in our work, again smaller compared to 10.00% and 5.22% for F18. However, they are larger than that of V18, possibly due to V18 analysing brighter stars, hence the light curves are less noisy. This can be seen by comparing the mean photometric flux error of the transit light curves fitted: 1007 parts per million (ppm) for this work, and 271 ppm for V18.

We select the planets in F18 that are in common with the planets in our sample, and examine the change in R_p . We find that 217 planets have a larger R_p after refitting, and smaller for 214 planets. Of the planets whose sizes have increased, the mean change is 9.79%, and

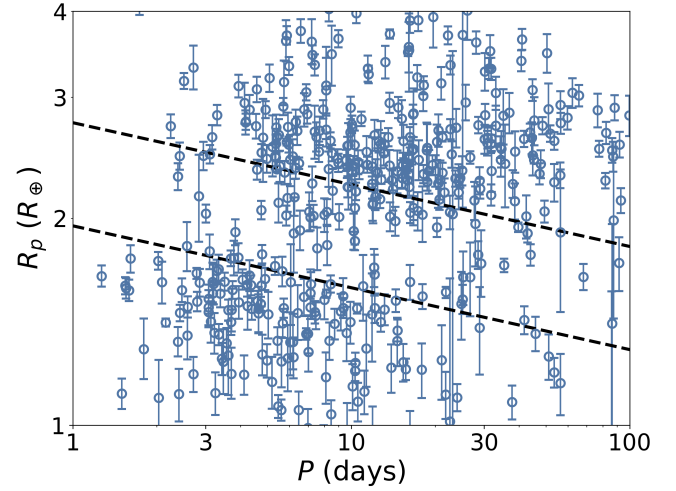


Figure 1. Radius-period plot of all 431 planets refitted in this work. The black dotted lines indicate the upper and lower boundaries of the radius valley defined in V18.

8.69% for planets with reduced sizes. Considering all 431 planets, our new results change R_p by a mean and median of only 0.62% and 0.02% respectively, indicating that our refitting results do not systematically alter the planet sizes. We observe that 120 planets (28%) have a revised $R_p > 2\sigma$ away from their corresponding values from F18, and 62 planets (14%) $> 3\sigma$ away.

3.2 Radius valley dependence on orbital period

To obtain the most precise planetary sample, we apply the following conservative cuts to our sample for subsequent analyses in the rest of this paper:

- (i) *Precision on R_p* : We exclude planets with a planet radius precision $\sigma_{R_p} > 10\%$.
- (ii) *Radius correction factor (RCF)*: We exclude planets with an RCF $> 5\%$, as reported in Furlan et al. (2017). RCFs may themselves be uncertain due to observational challenges in detecting nearby stellar companions and measuring their brightness (Furlan et al. 2017). Of the 137 planets with RCF measurements from Furlan et al. (2017), 18 (13%) have RCF $> 5\%$. The remaining 294 planets do not have RCF measurements currently available.
- (iii) *Number of transits*: We exclude planets with fewer than 3 transits in the *Kepler* short cadence data to limit the risk that correlated noise during an individual transit strongly affects the resulting fit.

After implementing these filters, 375 planets remain in our sample which we will use throughout the remainder of this work.

We first use this sample to investigate the location of the radius valley as a function of orbital period. Following the procedure outlined in Van Eylen et al. (2018), we calculate the position of the radius valley by determining the hyperplane of maximum separation. We perform this with a linear support-vector machine (SVM). To initialise our model, we initially classify our sample into two groups, ‘above’ and ‘below’ the radius valley on the radius-orbital period plane, by applying a Gaussian Mixture Model with two components in the R_p - P plane. Since the orders of magnitude of R_p and P are different, we divide P by 5 before applying the above clustering algorithm to allow the model to separate the planetary population into

Table 1. Table showing estimates of the orbital periods (P), planetary-to-stellar-radii ratio (R_p/R_\star), planetary radii (R_p), the number of transits in the fitted light curve (N_{tr}) of 431 planets refitted in this work. The source of R_\star to convert R_p/R_\star to R_p is listed in the References column: (1) [Fulton & Petigura \(2018\)](#), (2) [Van Eylen et al. \(2018\)](#). ‘Flag’ refers to whether the planet passes the filter checks and is included in the smaller subset for further analyses (1 for True and 0 for False). The complete list of parameters are provided in Appendix A. Only the first 10 planets are shown here; the full table is available online in a machine-readable format.

KOI	Kepler name	P (days)	R_p/R_\star	R_p (R_\oplus)	R_\star Source	N_{tr}	Flag
K00041.01	Kepler-100 c	12.815893 ± 0.000008	0.0138 ± 0.0002	$2.28^{+0.03}_{-0.03}$	(2)	93	1
K00041.02	Kepler-100 b	6.887062 ± 0.000007	0.0082 ± 0.0001	$1.36^{+0.03}_{-0.03}$	(2)	173	1
K00041.03	Kepler-100 d	35.333093 ± 0.000019	0.0104 ± 0.0002	$1.71^{+0.04}_{-0.04}$	(2)	35	1
K00046.02	Kepler-101 c	6.029792 ± 0.000020	0.0073 ± 0.0007	$1.32^{+0.14}_{-0.14}$	(1)	50	0
K00049.01	Kepler-461 b	8.313784 ± 0.000015	0.0287 ± 0.0010	$4.03^{+0.17}_{-0.17}$	(1)	34	1
K00069.01	Kepler-93 b	4.726739 ± 0.000001	0.0151 ± 0.0001	$1.50^{+0.04}_{-0.04}$	(2)	275	1
K00070.01	Kepler-20 A c	10.854089 ± 0.000003	0.0290 ± 0.0002	$2.79^{+0.07}_{-0.07}$	(1)	116	1
K00070.02	Kepler-20 A b	3.696115 ± 0.000001	0.0182 ± 0.0002	$1.75^{+0.05}_{-0.04}$	(1)	336	1
K00070.03	Kepler-20 A d	77.611598 ± 0.000019	0.0263 ± 0.0003	$2.52^{+0.07}_{-0.07}$	(1)	15	1
K00070.05	Kepler-20 A f	19.577627 ± 0.000020	0.0091 ± 0.0004	$0.88^{+0.04}_{-0.04}$	(1)	62	1
...

Table 2. Mean and median values radii determined in this work, [F18](#), and [V18](#). Values are listed as percentages (%).

Parameter		This work	F18	V18
Sample Size		431	1901	117
R_p/R_\star	Mean	4.76	8.73	3.20
	Median	3.44	4.07	2.44
R_\star	Mean	3.23	3.17	2.49
	Median	2.78	2.74	2.20
R_p	Mean	6.09	10.00	3.96
	Median	4.70	5.22	3.36

two groups above and below the radius valley. Otherwise, the population would be clustered in a way dominated by the difference in period. Following [Van Eylen et al. \(2018\)](#) and [David et al. \(2021\)](#), we select an SVM penalty parameter of $C = 10$ for the hyperplane, to minimise misclassification of data points above or below the radius valley, but still allow the hyperplane location to be determined by a sufficient number of data points. To determine accurate uncertainties on the location of the valley, we then perform a bootstrap by generating 1000 new sample sets on which we repeat the above procedure. Each bootstrap sample is generated by generating a new sample of the same size from the original sample, allowing replacement. Each bootstrapped sample is then categorised into two groups with a Gaussian Mixture Model, and the SVM procedure is repeated. Reporting the median value and taking the 16th and 84th percentiles as the upper and lower uncertainties, we find

$$\log_{10}(R_p/R_\oplus) = m \log_{10}(P/\text{days}) + c \quad (4)$$

with $m = -0.11 \pm 0.02$, and $c = 0.37^{+0.02}_{-0.03}$. The location of the radius valley is plotted in Fig. 2.

We also implement the method adopted by [Petigura et al. \(2022\)](#), which involves computing the planet density in the radius-period plane with a Gaussian kernel density estimate (KDE), and fitting the planet radius at the KDE minima between $\log_{10}(P/\text{days}) = 0.5 - 1.5$ (i.e. $P \approx 3.16 - 31.6$ days) and $\log_{10}(R_p/R_\oplus) = 0.15 - 0.35$ (i.e.

$R_p \approx 1.41 - 2.24R_\oplus$) according to equation 4, and performing bootstrap with 1000 sample sets to find the uncertainties. The result is illustrated in Figure 2. We use a KDE bandwidth of 0.467 in $\log_{10} P$ and 0.075 in $\log_{10} R_p$, which is based on the bandwidth used by [Petigura et al. \(2022\)](#), but scaled up linearly based on the ratios between the two sample sizes. We note that this method fits a narrower period range compared to the SVM method, which fits for the full $P = 1 - 100$ days. With this method, we obtain $m = -0.12^{+0.03}_{-0.05}$ and $c = 0.37^{+0.05}_{-0.03}$. We find this value to be slightly steeper than that determined with the SVM, however the two values are well within 1σ of each other. Here, we do not correct for detection completeness, and we note that this method is highly sensitive to the choice of the KDE bandwidth, and using a bandwidth five times larger results with a slope approximately twice as steep.

Some studies have opted to study the radius valley location as a function of incident flux S , in addition to, or instead of, P (e.g. [Rogers et al. 2021](#); [Petigura et al. 2022](#)). We calculate S according to the formula

$$S = \frac{L_\star}{4\pi a^2} \quad (5)$$

where L_\star is the host star’s luminosity. L_\star can itself be calculated using

$$L_\star = 4\pi R_\star^2 \sigma_{\text{sb}} T_{\text{eff}}^4 \quad (6)$$

where R_\star is the stellar radius, σ_{sb} is the Stefan-Boltzmann constant, and T_{eff} is the effective temperature of the star. Finally, a is the orbital semi-major axis, which is given by

$$\left(\frac{a}{R_\star}\right)^3 = \frac{GP^2 \rho_\star (1 + e \sin \omega)^3}{3\pi (1 - e^2)^{1.5}} \quad (7)$$

according to Kepler’s third law of planetary motion (e.g. [Van Eylen & Albrecht 2015](#); [Petigura 2020](#)). Here, G is the gravitational constant, P is the orbital period, ρ_\star is the stellar density, e and ω are the orbital eccentricity and argument of periapsis respectively. As before, we obtain the stellar properties (R_\star , ρ_\star , T_{eff}) from [V18](#) when available, and from [F18](#) otherwise. P , e , and ω are obtained from the transit fitting results of this work. Fitting the valley with the SVM, we obtain

Table 3. Dependencies of the radius valley in n dimensions (m_i), given by the equation $\log_{10}(R_p/R_\oplus) = \sum_{i=1}^n m_i x_i$, with different parameter combinations x_i . The methods used to obtain the equation of the radius valley hyperplanes are also given, where SVM and KDE stand for the support-vector machine and fitting the minima of the kernel density estimates respectively.

Dimensions	$\log_{10}(P/\text{days})$	$\log_{10}(S/S_\oplus)$	$\log_{10}(M/M_\odot)$	$\log_{10}(\text{Age/Gyr})$	[Fe/H]	Intercept	Method
2	$-0.11^{+0.02}_{-0.02}$					$0.37^{+0.02}_{-0.03}$	SVM
	$-0.12^{+0.03}_{-0.05}$					$0.37^{+0.05}_{-0.03}$	KDE
		$0.07^{+0.02}_{-0.01}$				$0.11^{+0.03}_{-0.04}$	SVM
			$0.23^{+0.09}_{-0.08}$			$0.27^{+0.01}_{-0.01}$	SVM
				$0.02^{+0.01}_{-0.02}$		$0.26^{+0.01}_{-0.01}$	SVM
3					$0.06^{+0.06}_{-0.08}$	$0.26^{+0.01}_{-0.01}$	SVM
	$-0.09^{+0.02}_{-0.03}$		$0.21^{+0.06}_{-0.07}$			$0.35^{+0.02}_{-0.03}$	SVM
		$0.07^{+0.02}_{-0.02}$	$-0.01^{+0.07}_{-0.09}$			$0.11^{+0.04}_{-0.05}$	SVM
	$-0.10^{+0.02}_{-0.02}$			$0.03^{+0.02}_{-0.03}$		$0.34^{+0.03}_{-0.02}$	SVM
4	$-0.10^{+0.03}_{-0.03}$				$0.03^{+0.03}_{-0.04}$	$0.36^{+0.02}_{-0.03}$	SVM
	$-0.096^{+0.023}_{-0.027}$		$0.231^{+0.053}_{-0.064}$	$0.033^{+0.017}_{-0.025}$		$0.339^{+0.026}_{-0.018}$	SVM

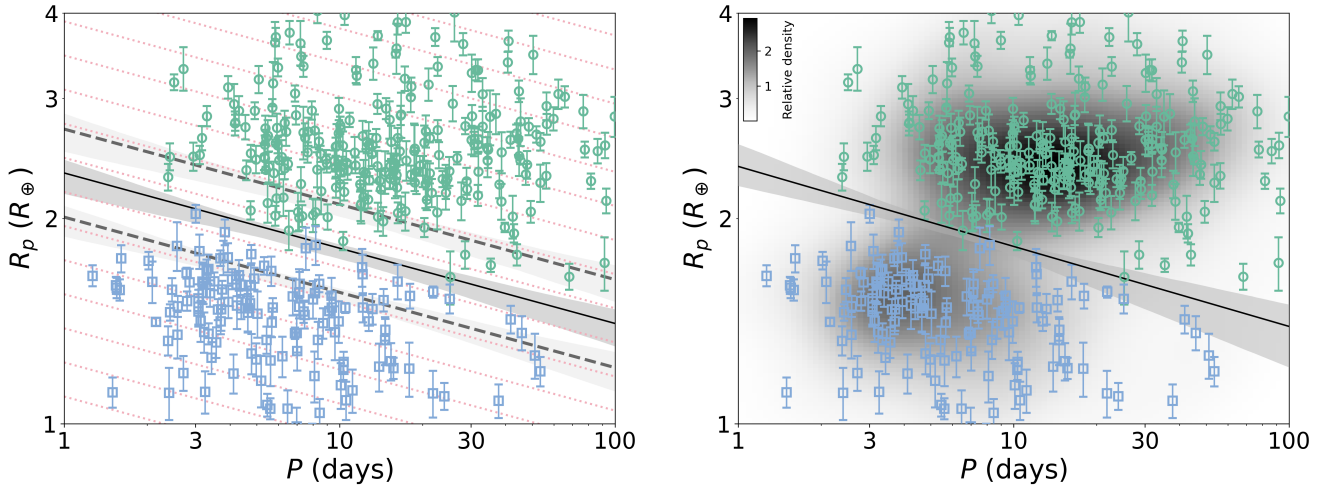


Figure 2. *Left:* Radius valley location determined with the support-vector machine (SVM), with $m = -0.11 \pm 0.02$, and $c = 0.36^{+0.02}_{-0.03}$, indicated by the black solid line. The dashed lines represent the median boundaries passing through the supporting vectors determining the position of the solid line. We define the area between the two lines as the radius valley region. The green and blue points show planets above and below the radius valley respectively. The grey shaded regions represent the $\pm 1\sigma$ uncertainties of the lines determined using the bootstrap method. The red dotted lines show the plot divided into multiple orbital-period dependent bins, which is then used for plotting the adjusted histogram in Fig. 4. *Right:* Radius valley position determined by fitting a line through the region where the kernel density estimate is minimum. With this method, we obtain $m = -0.12^{+0.03}_{-0.05}$, and $c = 0.37^{+0.0}_{-0.03}$, indicated by the black solid line with $\pm 1\sigma$ uncertainty shaded in grey.

$$\log_{10} R_p/R_\oplus = m \log_{10} S/S_\oplus + c \quad (8)$$

with $m = 0.07^{+0.02}_{-0.01}$, and $c = 0.11^{+0.03}_{-0.04}$. The location of the radius valley in terms of S is shown in Figure 3.

3.3 Depth of the radius valley

We investigate the depth of the radius valley. As we find the position of the radius valley is dependent on orbital period, we divide the radius valley into multiple tilted bins (as shown in Fig. 2 left) and

plot an adjusted histogram in logarithmic scale. We shift planets along the slope of the radius valley obtained with the SVM method in Section 3.2, i.e. $m = -0.11$, and plot a histogram of ‘expected’ planetary radii at an orbital period of 10 days, shown in Fig. 4. We choose to fit the histogram with a Gaussian Mixture Model of two clusters, as opposed to a Gaussian kernel density estimate, as the former is independent of the sizes and locations of the histogram bins, as well as the Gaussian bandwidth. Also, with the Gaussian Mixture Model, we are able to force the planets to fall into two groups only, matching the bimodal distribution of small planets.

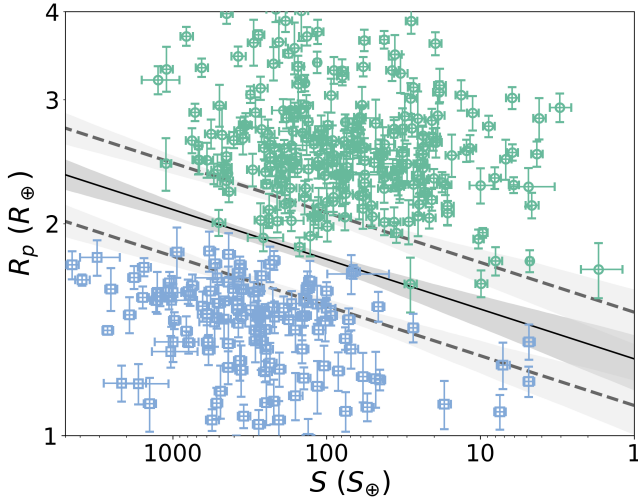


Figure 3. Same as Figure 2 left, but as a function of incident flux S instead of orbital period P .

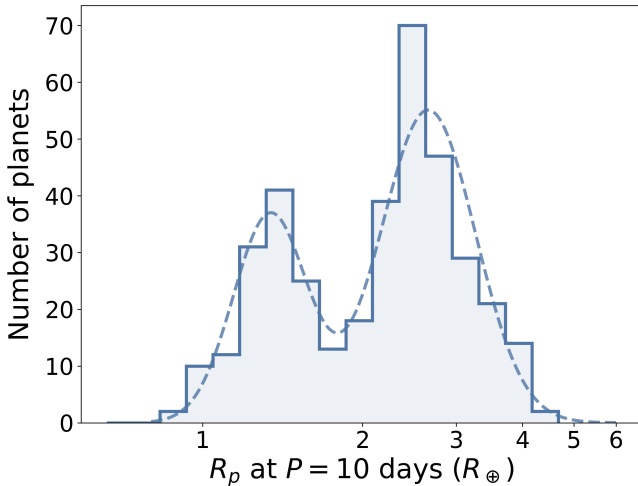


Figure 4. Histogram of planet radii, adjusted to equivalent radii at $P = 10$ days, according to the radius valley slope calculated in Section 3.2 with the SVM. Note that completeness corrections are not performed. Here, $E_{\text{avg}} = 2.98^{+0.60}_{-0.47}$.

Here, we propose the metric E , defined as

$$E_{\text{SN}} = N_{\text{sub-Neptune,peak}}/N_{\text{valley}} \quad (9)$$

and

$$E_{\text{SE}} = N_{\text{super-Earth,peak}}/N_{\text{valley}} \quad (10)$$

to compare the number of planets inside the valley and the peak number outside the valley. A higher E indicates a deeper radius valley. $N_{\text{sub-Neptune,peak}}$ and $N_{\text{super-Earth,peak}}$ are the number of planets at the sub-Neptune and super-Earth Gaussian peaks respectively, and N_{valley} is the number of planets at the lowest point between the two Gaussian peaks. As $N_{\text{sub-Neptune,peak}}$, $N_{\text{super-Earth,peak}}$, and N_{valley} are determined directly from the curve resulting from the Gaussian Mixture Model, this E metric is also independent of the histogram bin sizes or locations. To calculate the uncertainties of E , we again perform a bootstrap with 1000 sample sets, where each bootstrap

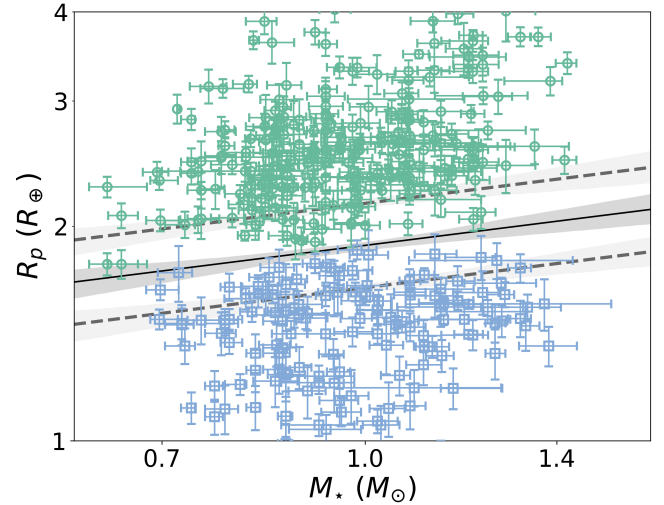


Figure 5. Plot of planetary radius against mass of host star. The solid line shows the location of the radius valley determined with the SVM, with slope $m = 0.23^{+0.09}_{-0.08}$, and $c = 0.27 \pm 0.01$. The dashed lines show the boundaries of the radius valley, given by the same m , and $c_{\text{upper}} = 0.33 \pm 0.01$, $c_{\text{lower}} = 0.22 \pm 0.01$. The shaded regions depict the $\pm 1\sigma$ uncertainties of the lines determined with bootstrapping.

sample is generated by generating a new sample of the same size from the original, allowing replacements. We also replace the radius of each selected planet by randomly drawing from a normal distribution with the reported planet radius as the mean, and the uncertainties on the radius as the variance. We report the median of this bootstrap distribution as our results, and the 84th and 16th percentiles as our $\pm 1\sigma$ uncertainties. We test this metric on known planetary samples on F18 and V18, which we know the difference in the radius valley depth, and find that their corresponding E value differ, hence demonstrating the reliability of such metric. The difference in the depth of the radius valley is further discussed in Section 4.3. We find that for our new short cadence results, the ratios are $E_{\text{SN}} = 3.59^{+0.77}_{-0.62}$ and $E_{\text{SE}} = 2.40^{+0.61}_{-0.41}$. Averaging the two numbers gives us $E_{\text{avg}} = 2.98^{+0.60}_{-0.47}$.

3.4 Radius valley dependence on stellar mass

We investigate the radius valley location as a function of stellar mass. We first implement a 2-dimensional SVM, using the same method as in Section 3.2. The result is shown in Figure 5. We find $d \log R_p / d \log M_{\star} = 0.23^{+0.09}_{-0.08}$, and the intercept $c = 0.27 \pm 0.01$.

Rogers et al. (2021) suggested the degeneracy between the photo-evaporation and core-powered mass loss scenarios could be broken with an analysis of the radius valley in 3 dimensions. Hence, we implement an SVM in 3 dimensions: planet radius R_p , orbital period P , and mass of the host star M_{\star} , to fit the radius valley in the form of a plane. We perform bootstrapping with 1000 sample sets as per previous. We obtain the relation

$$\log_{10}(R_p/R_{\oplus}) = A \log_{10}(P/\text{days}) + B \log_{10}(M_{\star}/M_{\odot}) + C \quad (11)$$

with $A = -0.09^{+0.02}_{-0.03}$, $B = 0.21^{+0.06}_{-0.07}$, $C = 0.35^{+0.02}_{-0.02}$. An illustration of the SVM plane is shown in Figure 6.

We also investigate the radius valley location in the R_p - S - M_{\star} space. Figure 6 right shows the radius valley location in this space.

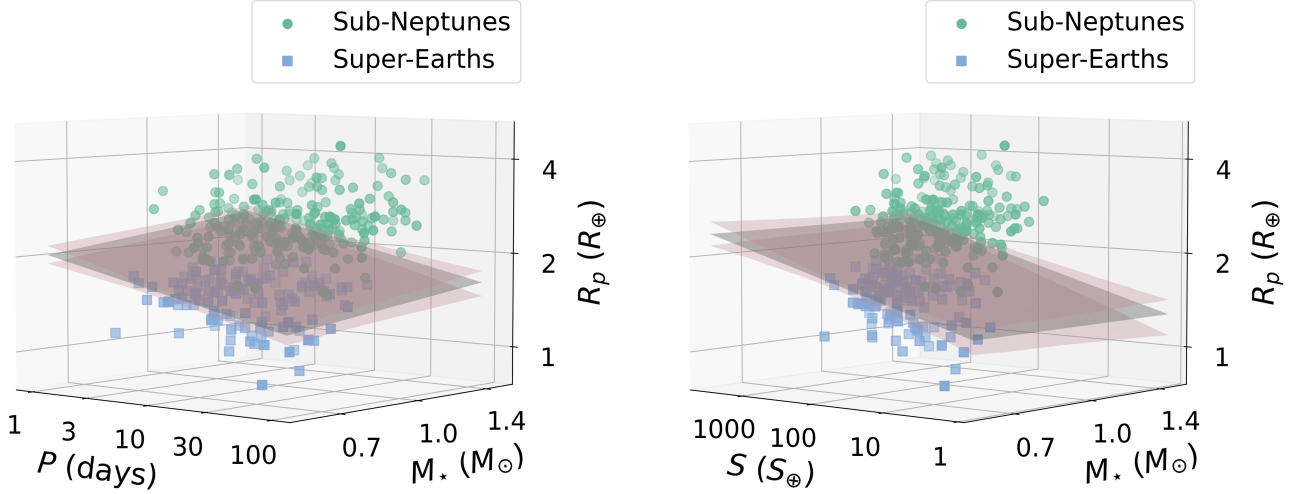


Figure 6. Plot of planet radius against orbital period and mass of host star (left), and planet radius against incident flux and stellar mass (right). The grey plane shows the radius valley location determined with the SVM in 3 dimensions, with the $\pm 1\sigma$ uncertainties shown in pink. The uncertainties on individual planet parameters are not displayed in the interest of clarity.

We find

$$\log_{10}(R_p/R_\oplus) = A \log_{10}(S/S_\oplus) + B \log_{10}(M_\star/M_\odot) + C \quad (12)$$

with $A = 0.07 \pm 0.02$, $B = -0.01^{+0.07}_{-0.09}$, and $C = 0.11^{+0.04}_{-0.05}$.

3.5 Radius valley dependence on stellar age

We investigate the location of the radius valley as a function of stellar age. We obtain the stellar ages from F18. Kepler-174 does not have stellar age data from this source, hence we omit Kepler-174 b and Kepler-174 c in our analysis with stellar age.

Fitting the valley with the SVM, we obtain

$$\log_{10}(R_p/R_\oplus) = m \log_{10}(\text{Age/Gyr}) + c \quad (13)$$

with $m = 0.02^{+0.01}_{-0.02}$, $c = 0.26^{+0.01}_{-0.01}$, showing no significant correlation with the radius valley location in 2-dimensional space. The result is displayed in Figure 7 (left panel).

We further investigate whether the radius valley *depth* may be a function of stellar age. To do so we generate histograms, similar to Figure 4, split into different stellar age subsamples. Figure 8 (left panel) shows that for older stars, the radius valley location shifts to higher R_p , and the radius valley becomes shallower. The change in the E metric is reported in Table 4. These findings suggest that the radius valley has a dependence on the age of the host stars.

We further plot the radius valley in R_p - P -age space, and fit the valley with the SVM, as shown in Figure 9 (left panel). We find

$$\log_{10}(R_p/R_\oplus) = A \log_{10}(P/\text{days}) + B \log_{10}(\text{Age/Gyr}) + C \quad (14)$$

with $A = -0.10 \pm 0.02$, $B = 0.03^{+0.02}_{-0.03}$, and $C = 0.34^{+0.03}_{-0.02}$.

We can also combine R_p , P , M_\star , and stellar age, and determine the radius valley with a 4-dimensional SVM, as shown in Figure 10. The resulting equation representing the radius valley is in the form of a 4-dimensional hyperplane

$$\log_{10}(R_p/R_\oplus) = A \log_{10}(P/\text{days}) + B \log_{10}(M_\star/M_\odot) + C \log_{10}(\text{Age/Gyr}) + D \quad (15)$$

Table 4. E values of the radius valley for different ages of the host stars. $E_{\text{avg}} = (E_{\text{SN}} + E_{\text{SE}})/2$.

$\log_{10}(\text{Age/yr})$	Age (Gyr)	N_{planets}	E_{SN}	E_{SE}	E_{avg}
< 9.25	< 1.78	53	4.93	3.64	4.28
9.25 – 9.5	1.78 – 3.16	95	4.69	3.08	3.89
9.5 – 9.75	3.16 – 5.62	114	3.22	3.32	3.27
> 9.75	> 5.62	111	2.21	4.40	3.30

with $A = -0.096^{+0.023}_{-0.027}$, $B = 0.231^{+0.053}_{-0.064}$, $C = 0.033^{+0.017}_{-0.025}$, $D = 0.339^{+0.026}_{-0.018}$. These results imply there is strong evidence the radius valley location is dependent on P and M_\star , and weak evidence for its dependence on stellar age ($> 1\sigma$). These values are also consistent within 1σ with their corresponding dependencies in two and three dimensions (see Table 3).

3.6 Radius valley dependence on stellar metallicity

We perform a similar analysis in terms of the stellar metallicity. As for age, we obtain the stellar metallicity from V18 if available, and F18 otherwise. We find

$$\log_{10}(R_p/R_\oplus) = m[\text{Fe}/\text{H}] + c \quad (16)$$

with $m = 0.06^{+0.06}_{-0.08}$, $c = 0.26^{+0.01}_{-0.01}$, again displaying no significant correlation with the radius valley location in 2-dimensional space.

We divide the planet population into two groups, based on the median $[\text{Fe}/\text{H}] = 0.06$. The adjusted histograms in Figure 8 (right panel) show that the super-Earth peak is lower for metal-poor stars. The E values are reported in Table 5.

We perform a similar SVM analysis in R_p - P - $[\text{Fe}/\text{H}]$ space (shown in Figure 9 right panel), and find

$$\log_{10}(R_p/R_\oplus) = A \log_{10}(P/\text{days}) + B[\text{Fe}/\text{H}] + C \quad (17)$$

with $A = -0.10 \pm 0.03$, $B = 0.03^{+0.03}_{-0.04}$, and $C = 0.36^{+0.02}_{-0.03}$. These

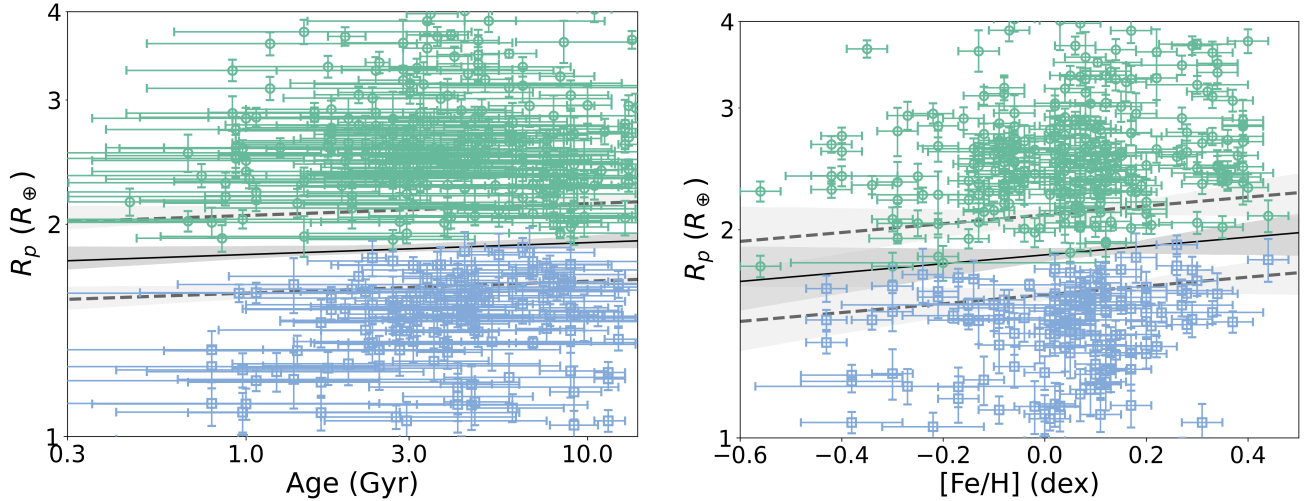


Figure 7. Same as Figure 5, but for stellar age (left, $m = 0.01^{+0.01}_{-0.02}$, $c = 0.26^{+0.01}_{-0.01}$), and stellar metallicity [Fe/H] (right, $m = 0.06^{+0.06}_{-0.08}$, $c = 0.26^{+0.01}_{-0.01}$).

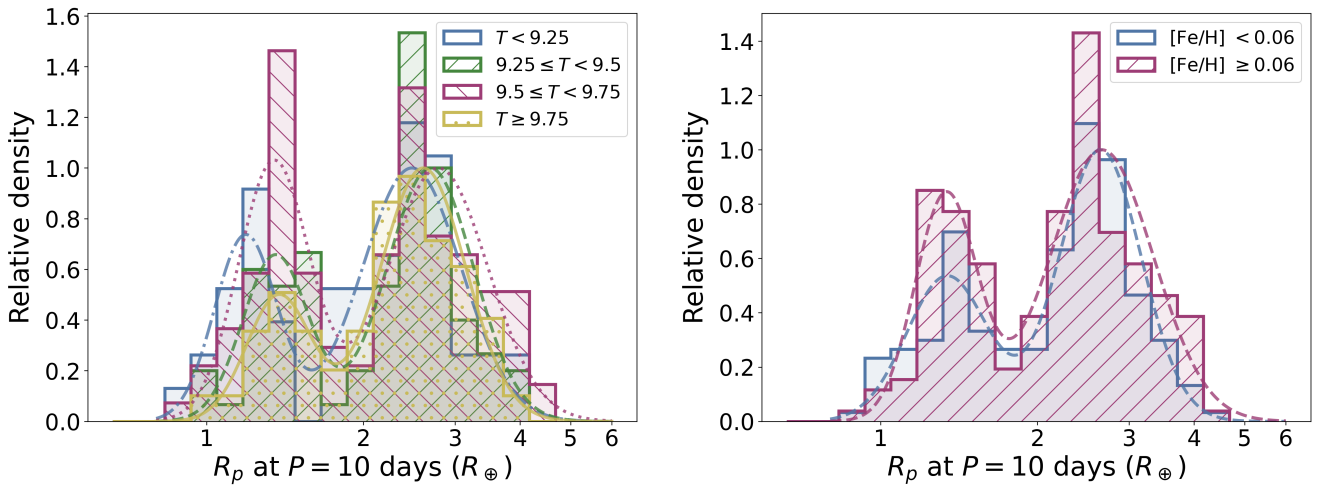


Figure 8. Same as Figure 4, but separated into different stellar ages (left), and metallicities (right). Here, $T = \log_{10}(\text{Age/yr})$. The histograms are normalised such that the relative density of the sub-Neptune peak equals to unity.

Table 5. E values of the radius valley for different stellar metallicities. $E_{\text{avg}} = (E_{\text{SN}} + E_{\text{SE}})/2$.

[Fe/H]	N_{planets}	E_{SN}	E_{SE}	E_{avg}
< 0.06	181	4.10	2.20	3.15
≥ 0.06	194	3.28	2.78	3.03

values imply that we find no evidence that the radius valley location depends on stellar metallicity.

4 DISCUSSION

4.1 R_p - P relation suggests a thermally-driven mass loss model

As presented in Section 3.2, we observe the radius valley scales as $m = d \log R_p / d \log P = -0.11 \pm 0.02$. This negative period-dependence is a robust finding which remains roughly similar even when other parameters are included in the fit (see Table 3).

Different theoretical mechanisms to create the radius valley result in a different slope as a function of orbital period. For example, [Lopez & Rice \(2018\)](#) predicted that if the rocky planets are core remnants of sub-Neptunes with evaporated atmospheres, the radius valley location should decrease with increasing orbital period, with $m = -0.09$, whereas if those rocky planets were formed after disk dissipation (i.e., late gas-poor formation), the radius valley location tends to larger planetary radii at longer orbital periods, with $m = 0.11$. Similarly, [Owen & Wu \(2017\)](#) predicted a negative period-radius valley slope for a photoevaporation model, with $-0.25 \leq m \leq -0.16$ depending on the photoevaporation efficiency. If the radius valley is thermally driven but powered by the core rather than photoevaporation, the slope would be similarly negative, with e.g., [Gupta & Schlichting \(2019\)](#) predicting that $m \approx -0.11$ in this case. Theoretically predicted slopes for different formation mechanisms are summarised in Table 6.

Our observed negative slope is consistent with thermally driven mass-loss models but inconsistent with late gas-poor models. We can also compare our observed slope with other observational

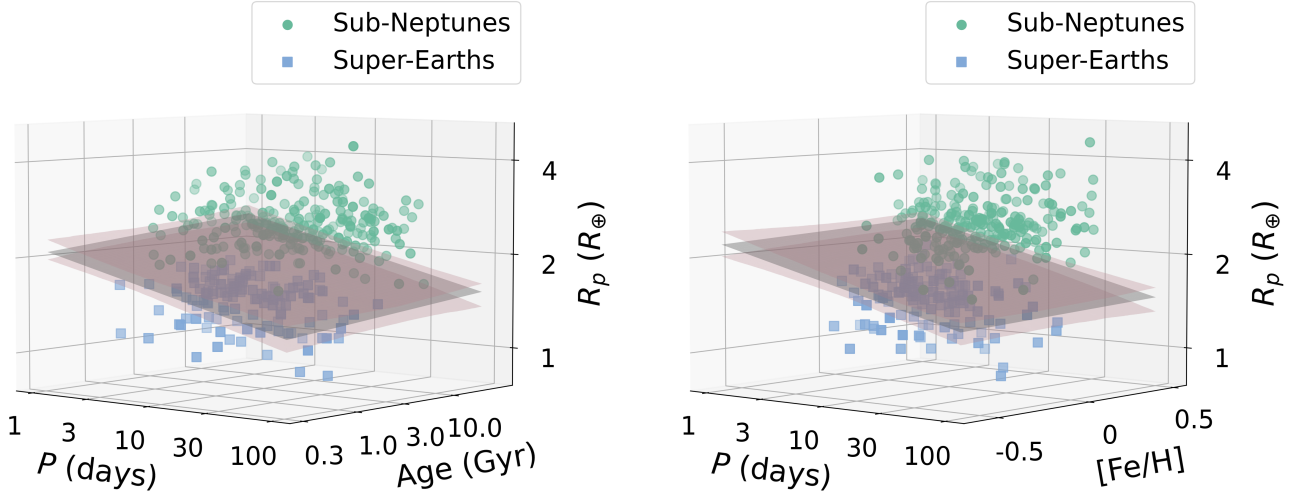


Figure 9. Same as Figure 6, but in R_p – P –age space (left) and R_p – P – $[\text{Fe}/\text{H}]$ space (right).

Table 6. Slope of the radius valley on the radius–period plane from various sources.

	Source	$m = d \log R_p / d \log P$	Stellar type
Observations	This work	$-0.11^{+0.02}_{-0.02}$	FGK
	Van Eylen et al. (2018)	$-0.09^{+0.02}_{-0.04}$	FGK
	Martinez et al. (2019)	$-0.11^{+0.02}_{-0.02}$	FGK
	MacDonald (2019)	$-0.319^{+0.088}_{-0.116}$	FGK
	Cloutier & Menou (2020)	$0.058^{+0.022}_{-0.022}$	M
	Van Eylen et al. (2021)	$-0.11^{+0.05}_{-0.04}$	M
	Petigura et al. (2022)	$-0.11^{+0.02}_{-0.02}$	FGKM
	Luque & Pallé (2022)	$-0.02^{+0.05}_{-0.05}$	M
	Source	$m = d \log R_p / d \log P$	Model
Theory	Owen & Wu (2017)	$-0.25 \leq m \leq -0.16$	Photoevaporation
	Lopez & Rice (2018)	-0.09	Photoevaporation
	Gupta & Schlichting (2019)	0.11	Gas-poor formation
	Rogers et al. (2021)	-0.11	Core-powered mass loss
			-0.16
		-0.11	Core-powered mass loss

studies (see again Table 6). The period–radius slope was first observed by Van Eylen et al. (2018), who used the SVM approach that we adopted here and who found $m = -0.09^{+0.02}_{-0.04}$. A different approach was followed by Martinez et al. (2019), who divided their planetary sample into 10 bins with equal number of planets, determined the minimum radius in each bin, and fitted a linear relationship to obtain equation 4. These two approaches led to a consistent result, with $m = -0.11 \pm 0.02$. MacDonald (2019) adopted machine learning approaches, and report $m = -0.319^{+0.088}_{-0.116}$. The above studies all focus on samples of FGK stars, where various approaches to model the valley’s location appear to result in negative slopes with consistent magnitude, matching thermally-driven atmospheric loss models.

For smaller and cooler (M type) stars, Cloutier & Menou (2020) found a positive slope ($m = 0.058 \pm 0.022$) using a method similar

to Martinez et al. (2019), suggesting for these stars the valley may be the result of gas-poor formation rather than being thermally driven. Van Eylen et al. (2021) used the SVM approach to measure the M dwarf valley and found a negative slope instead, of $-0.11^{+0.05}_{-0.04}$. Luque & Pallé (2022) used the `gapfit` package (Lloyd et al. 2020) and found $m = -0.02 \pm 0.05$. A recent study by Petigura et al. (2022) also included M type stars in addition to FGK stars, and they found $m = -0.11 \pm 0.02$ for this sample. Our sample does not include M type stars but does span a mass range from about 0.6 to 1.4 M_\star .

To investigate whether the slope of m changes with stellar mass within our sample, we split our planetary sample into two groups: $M_\star \geq 1M_\odot$, and $M_\star < 1M_\odot$. We determine the R_p – P relation separately for these two groups with the same methods as above. We find for $M_\star \geq 1M_\odot$, $m = -0.07^{+0.02}_{-0.04}$ and $c = 0.35^{+0.03}_{-0.02}$, for

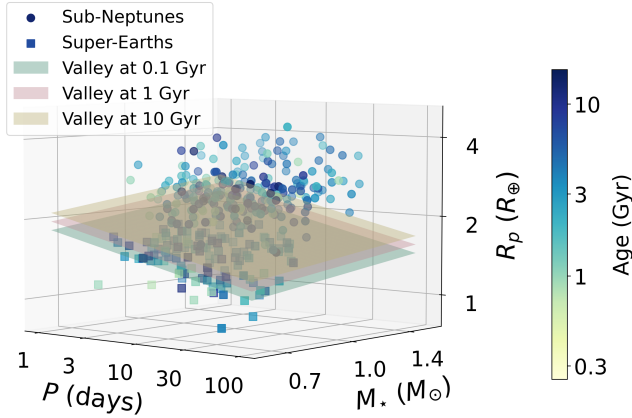


Figure 10. Radius valley location in terms of orbital period, stellar mass, and stellar age. The colour bar represents the age of the planetary host stars, and planes of different colours indicate the radius valley location for different stellar ages.

$M_{\star} < 1M_{\odot}$, $m = -0.11^{+0.02}_{-0.07}$ and $c = 0.35^{+0.05}_{-0.02}$. These results are shown in Figure 11. The two values are in agreement within 1σ , suggesting that within our sample the radius valley location as a function of orbital period is inconsistent with the gas-poor formation scenario.

We can also look at the slope of the valley as a function of incident flux (S) rather than orbital period. By Kepler’s third law (as shown in equation 7), planets at longer orbital periods are located further away from the planet, thus the incident flux S is lower for planets with larger star-planet distances as shown in equation 5. Hence, we expect for a thermally-driven planetary mass loss scenario, the radius valley location tends to larger planetary radii for higher S . We observe this positive relationship in this work, in agreement with other previous observations as shown in Table 7, and consistent with thermally-driven mass loss models which is also shown in radius-period space.

4.2 R_p - M_{\star} relation supports a thermally-driven mass loss model

As presented in Section 3.4, we find that in two dimensions, $m = d \log R_p / d \log M_{\star} = 0.23^{+0.09}_{-0.08}$.

A stellar mass dependence has been predicted by radius valley models. Both thermally driven mass-loss models predict a similar dependence of the valley on stellar mass. For example, Rogers et al. (2021) predicted $m = 0.29$ and $m = 0.32$ for photoevaporation (Owen & Wu 2017) and core-powered mass loss models (Gupta & Schlichting 2019, 2020) respectively. Our results are consistent with both sets of models within 1σ .

A stellar mass dependence was observed by Berger et al. (2020), who find $m = 0.26^{+0.21}_{-0.16}$ by fitting the minima of the 2-dimensional KDE in $R_p - M_{\star}$ space. A recent study by Petigura et al. (2022), similarly following a binning approach and incorporating data from Data Release 2 (DR2) of the California-Kepler Survey (CKS) for cooler stars, estimated $m = 0.18^{+0.08}_{-0.07}$. It is therefore reassuring to see that despite the different method adopted here, the slope derived in this work is consistent with both of these studies within 1σ . For lower mass stars, Luque & Pallé (2022) found $m = 0.08 \pm 0.12$; this may be inconsistent with our results at 1σ , however the stellar mass

range they studied is significantly lower than that in our sample with no overlaps. The results are summarised in Table 8.

When extending our analysis to 3 dimensions as a function of P and M_{\star} , we obtain $A = (\partial \log R_p / \partial \log P)_{M_{\star}} = -0.09^{+0.02}_{-0.03}$, $B = (\partial \log R_p / \partial \log M_{\star})_P = 0.21^{+0.06}_{-0.08}$ from determining the radius valley location in the R_p - P - M_{\star} space. Note that this is different to the total derivative $d \log R_p / d \log M_{\star}$ in two dimensions (shown in Table 3). Based on the models of photoevaporation (Owen & Wu 2017; Owen & Adams 2019; Mordasini 2020) and core-powered mass loss (Gupta & Schlichting 2019, 2020), Van Eylen et al. (2021) predicted $B = 0.19$ for a photoevaporation model, and $B = 0.33$ for a core-powered mass-loss model. Our resulting posterior distribution of A and B determined from the bootstrapping presented in Section 3.4, as shown in Figure 12, is consistent with both the photoevaporation and core-powered mass loss cases at 2σ , hence we are unable to distinguish between the two models in this particular parameter space.

Rogers et al. (2021) proposed an analysis of the radius valley in R_p - S - M_{\star} space that could distinguish between the two different thermally-driven mass-loss mechanisms. Using theoretical models, they predicted the radius valley scales as a function of S and M_{\star} as equation 11, with $A = (\partial \log R_p / \partial \log S)_{M_{\star}} \simeq 0.12$ and $B = (\partial \log R_p / \partial \log M_{\star})_S \simeq -0.17$ for a photoevaporation model, and $A \simeq 0.08$ and $B \simeq 0.00$ for a core-powered mass loss model. Again, we plot the posterior distributions of A and B as shown in Figure 13, and observe that our results are consistent with the core-powered mass loss case well within 1σ . For the photoevaporation scenario, our values overlap with the theoretical predictions at the edge of the 2σ confidence interval. Rogers et al. (2021) also measured the planet density of the California-Kepler Survey (CKS, Fulton & Petigura 2018), and the Gaia-Kepler Survey (GKS, Berger et al. 2020), in R_p - S - M_{\star} space. They found for the CKS data, $A = 0.13^{+0.03}_{-0.05}$, $B = -0.21^{+0.33}_{-0.39}$, and for the GKS data, $A = 0.10^{+0.03}_{-0.02}$, $B = -0.03^{+0.10}_{-0.12}$. Our results are in agreement with both the CKS and GKS values, and our measurements have smaller uncertainties.

There are some caveats to this comparison between our observation results and theoretical models. Firstly, the thermally-driven mass loss models predict the slope of the bottom of the valley (Van Eylen et al. 2018; Rogers et al. 2021), whereas our SVM finds the slope for the middle of the radius valley. Some studies have suggested a different planet size dependence with orbital period for super-Earths and sub-Neptunes (e.g. Petigura et al. 2022), hence these two slopes may not be equal. Since the radius valley is not completely empty, the bottom of the radius valley is not clearly defined, and there would be challenges locating and fitting the bottom of the radius valley. As a result, our observed values may not be fully comparable with theoretical model values. Furthermore, the method of extracting the radius valley is prone to transit biases, which we do not correct for in this work. Rogers et al. (2021) showed that even when modelling synthetic transit surveys based on evolving planets with theoretical models, the resulting posteriors may not be fully consistent with the theoretically predicted slope. Further work, such as generating synthetic surveys from both photoevaporation and core-powered mass loss models based on conditions similar to that of our sample in a method similar to that performed in Rogers et al. (2021), and fitting the valley with the same method as in this work, or analysing more planets around stars in a larger mass range, is required to compare our observations to theoretical models in a homogeneous way.

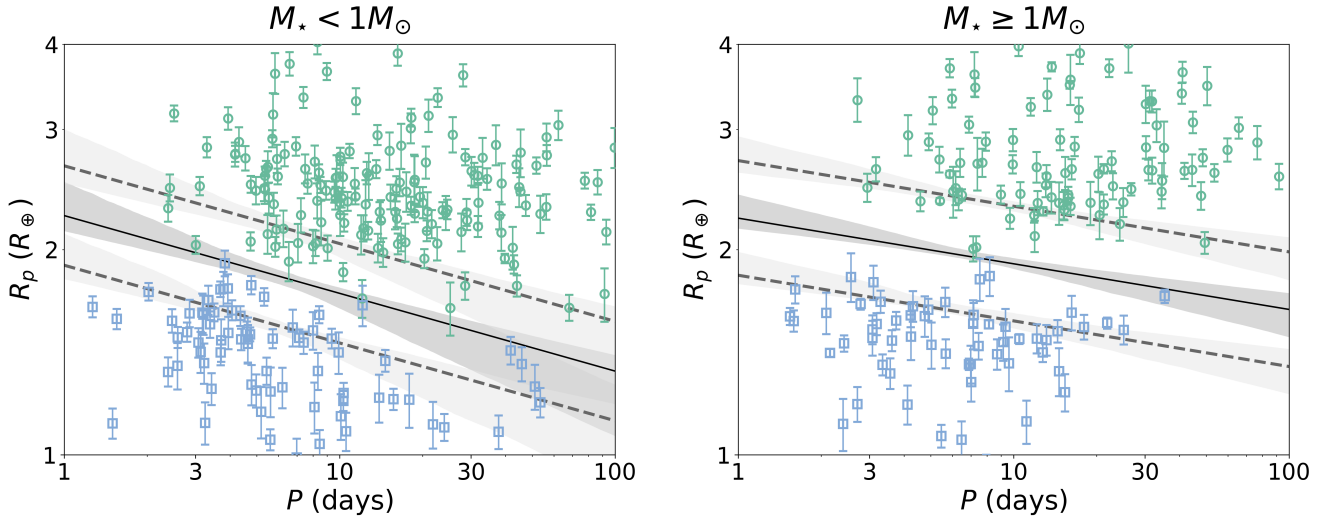


Figure 11. Radius valley position for planets with host star mass $M_\star < 1M_\odot$ (left), and $M_\star \geq 1M_\odot$ (right). For $M_\star < 1M_\odot$, $m = -0.11^{+0.02}_{-0.07}$ and $c = 0.35^{+0.05}_{-0.02}$, for $M_\star \geq 1M_\odot$, $m = -0.07^{+0.02}_{-0.04}$ and $c = 0.35^{+0.03}_{-0.02}$. The green and blue points show planets above and below the radius valley respectively. The grey shaded region represents the $\pm 1\sigma$ uncertainty in the radius valley position determined with bootstrapping.

Table 7. Same as Table 6, but for the radius valley slope on the radius-incident-flux plane.

	Source	$m = d \log R_p / d \log S$	Stellar type
	This work	$0.07^{+0.02}_{-0.01}$	FGK
	Martinez et al. (2019)	0.12 ± 0.02	FGK
Observations	Cloutier & Menou (2020)	-0.060 ± 0.025	M
	Petigura et al. (2022)	0.06 ± 0.01	FGKM
	Luque & Pallé (2022)	0.02 ± 0.02	M

Table 8. Same as Table 6, but for the radius valley slope on the radius-stellar-mass plane.

	Source	$m = d \log R_p / d \log M_\star$	Stellar type
	This work	$0.23^{+0.09}_{-0.08}$	FGK
Observations	Berger et al. (2020)	$0.26^{+0.21}_{-0.16}$	FGKM
	Petigura et al. (2022)	$0.18^{+0.08}_{-0.07}$	FGKM
	Luque & Pallé (2022)	$0.08^{+0.12}_{-0.12}$	M
	Source	$m = d \log R_p / d \log M_\star$	Model
Theory	Gupta & Schlichting (2020)	0.33	Core-powered mass loss
	Rogers et al. (2021)	0.29	Photoevaporation
		0.32	Core-powered mass loss

4.3 Deeper radius valley suggests a homogeneous initial planetary core composition

We now turn to the depth of the radius valley. Using the previously defined depth metric (E , equations 9 and 10), we find a valley depth of $E_{\text{avg}} = 2.98^{+0.60}_{-0.47}$ (see Section 3.3). We can compare this depth to the valley observed by F18. Shifting the planets along the slope calculated in Section 3.2, and applying the same metric to their filtered sample of 907 planets, we calculate $E_{\text{SN}} = 1.99^{+0.26}_{-0.23}$, $E_{\text{SE}} = 2.28^{+0.31}_{-0.27}$, giving $E_{\text{avg}} = 2.14^{+0.26}_{-0.21}$ for that sample. For V18, we shift the planets according to the slope obtained in their study, i.e.

$m = -0.09^{+0.02}_{-0.04}$, and we find $E_{\text{SN}} = 7.11^{+4.70}_{-2.49}$, $E_{\text{SE}} = 4.75^{+3.42}_{-1.70}$, giving $E_{\text{avg}} = 6.05^{+3.87}_{-2.14}$. These values imply that compared to F18, we observe a deeper radius valley. On the other hand, the radius valley appears less deep than observed by V18 for a smaller sample. This finding is visualised in Figure 14, which shows the adjusted histograms of the sample studied here next to the F18 and the V18 samples.

To investigate the reason for observing a deeper valley than F18, we compare the 211 planets common in both our sample and the filtered sample of F18. To investigate the role of transit fitting, we convert

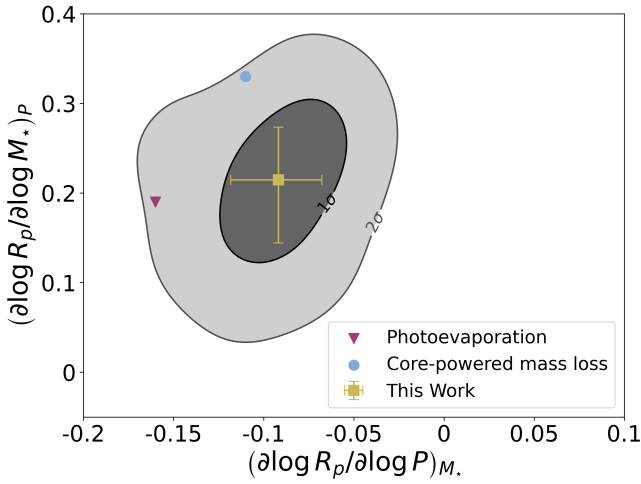


Figure 12. Posterior distributions of the radius valley location dependence with respect to orbital period at constant stellar mass $(\partial \log R_p / \partial \log P)_{M_\star}$, and stellar mass at constant orbital period $(\partial \log R_p / \partial \log M_\star)_P$. The dark and light-coloured shades represent the 1σ and 2σ uncertainties respectively. The theoretical models of photoevaporation and core-powered mass loss are taken from [Van Eylen et al. \(2021\)](#).

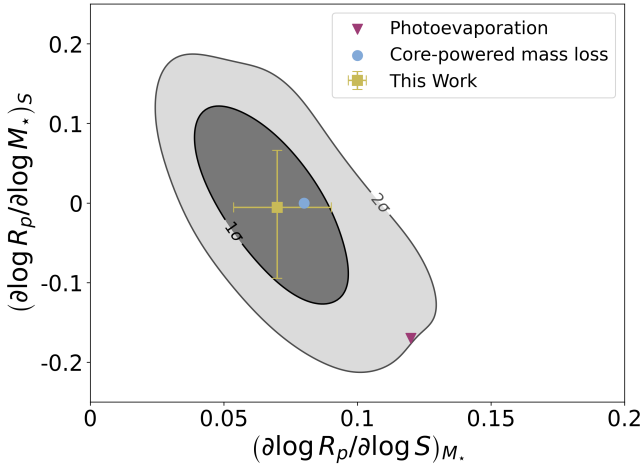


Figure 13. Same as Figure 12, but for $(\partial \log R_p / \partial \log S)_{M_\star}$ and $(\partial \log R_p / \partial \log M_\star)_S$.

all our R_p/R_\star into R_p using R_\star from [F18](#) (even when [V18](#) values are available). The results are shown in Figure 15, which compares the same planets with the same stellar parameters but different transit fitting. We observe that in this case, the R_p of 56 (27%) and 24 (11%) planets change by $> 2\sigma$ and $> 3\sigma$ respectively, compared to the values reported in [F18](#). We find for this common planetary sample, for our planetary parameters, $E_{\text{SN}} = 3.63^{+1.02}_{-0.70}$, $E_{\text{SE}} = 2.95^{+0.86}_{-0.63}$, giving $E_{\text{avg}} = 3.29^{+0.91}_{-0.59}$, whereas for parameters from [F18](#), $E_{\text{SN}} = 2.40^{+0.59}_{-0.47}$, $E_{\text{SE}} = 1.93^{+0.49}_{-0.39}$, giving $E_{\text{avg}} = 2.18^{+0.49}_{-0.42}$. These findings suggest that our updated transit fittings are directly responsible for deepening (although not fully emptying) the radius valley.

A deeper radius valley is associated with a more homogeneous planet core composition. For example, in photoevaporation models the radius valley position is dependent on the mass of the planet core

(M_c), and the density of a $1M_\oplus$ core of a particular core composition (ρ_{M_\oplus}), as

$$R_{\text{valley}} \propto \rho_{M_\oplus}^{-1/3} M_c^{1/4}. \quad (18)$$

Hence, if R_{valley} is known, and the planets' mean masses are known, the planetary core compositions could be deduced ([Owen & Wu 2017](#)).

Using the above relation, if the planetary cores were icy at formation, the radius valley would be located at a higher planetary radius than if the cores were rocky/terrestrial at formation. Hence, if the planetary cores are of mixed composition, a superposition of the two models would be predicted, and we would expect the radius valley to be smeared and less distinct, as each type of planet would have its own 'radius valley' at a different location ([Owen & Wu 2017](#)). Our deep radius valley found in this work implies the opposite case, where the planetary cores are more similar in composition. In this scenario, planets inside the valley may have a different (e.g. icy) composition.

[Owen & Wu \(2017\)](#) compared their models to observations, and found that the planet compositions are more likely to be Earth-like (i.e. rocky), but that the apparent shallowness of the valley suggested a wide distribution of iron fractions (f_{Fe}) in their cores, as planets with a single value iron fraction ($f_{\text{Fe}} = 0.5$) produces a deeper valley compared to planets with a uniform distribution ($f_{\text{Fe}} \in [0, 1]$). Comparing our finding of a deeper valley to models in [Owen & Wu \(2017\)](#) would indicate that the planet compositions are more likely to have similar iron fractions with a narrower spread.

Similarly, in the core-powered mass loss model, the location of the radius valley scales as

$$R_{\text{valley}} \propto \rho_c^{-4/9} \quad (19)$$

where ρ_c is the planet core density ([Gupta & Schlichting 2019](#)). The same reasoning as the photoevaporation case then applies: given the larger ρ_c for icy cores, planets with homogeneous icy cores will produce a radius valley at a larger planetary radii compared to rocky/terrestrial cores, implying that the radius valley would be smeared if planetary cores are of inhomogeneous compositions. Our deep radius valley supports the opposite case, i.e., a similar planetary core composition.

Figure 16 shows the stellar parameter distributions for the planet host stars in the three planet samples, and the mean and median values are listed in Table 9. We notice a similar stellar parameter range between this work and [F18](#), however the stars in [V18](#) are brighter, have a larger mean radius and mass, and higher effective temperature. This is likely due to [V18](#) selecting stars which display strong asteroseismic signals, which usually are brighter and larger stars. This observation may indicate that the radius valley of such stars are emptier, however the details are left for future studies.

Despite our new results revealing that the radius valley deepens by refitting planets with 1-minute short cadence light curves, it is still uncertain whether the difference between results from this work and [F18](#) is solely due to the cadence in transit data used, as different methods are used in the transit fitting process. [Mullally et al. \(2015\)](#) fitted planets using the method described in [Rowe et al. \(2014\)](#), which first fits a multi-planet transit model to the light curves, with fixed limb darkening parameters from [Claret & Bloemen \(2011\)](#), and subsequently fitting for each planet in a system independently by removing photometric contributions of other planets based on the parameters from the multi-planet fit. In our work, we fit planets in multi-planet systems simultaneously, such that each system shares the same stellar parameters including limb-darkening parameters and stellar density.

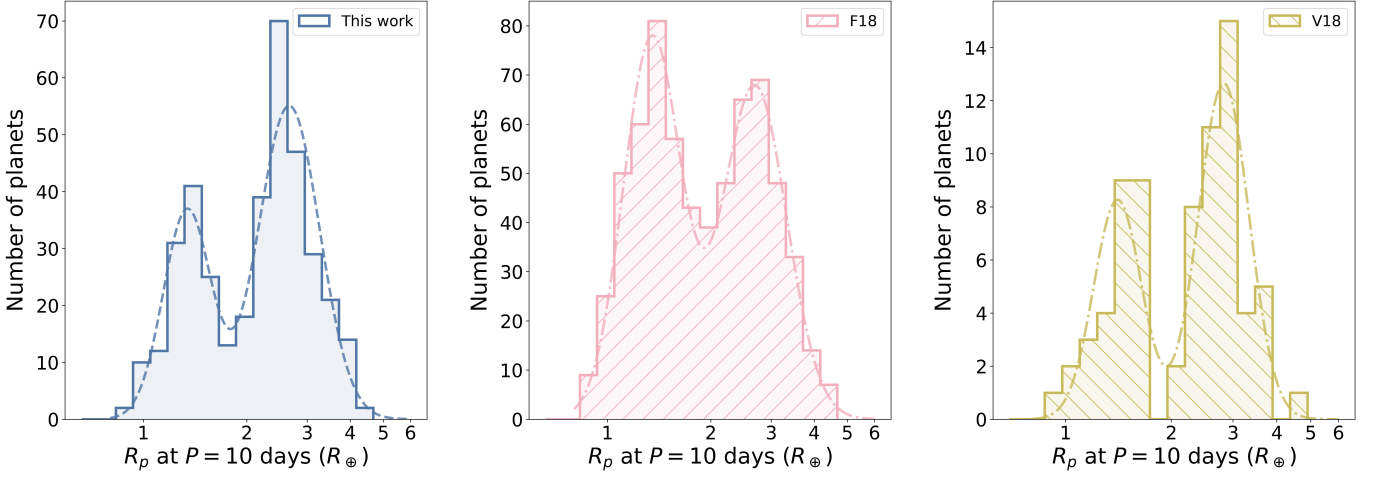


Figure 14. Histogram of planet radii, adjusted to $P = 10$ days for the planetary population in this work (left, identical to Figure 4), F18 (centre), and V18 (right). Planets in this work and F18 are shifted according to the slope defined in Section 3.2 with the SVM (i.e. $-0.11^{+0.02}_{-0.02}$), whereas planets in V18 are shifted according to the slope found in V18 (i.e. $m = -0.09^{+0.02}_{-0.04}$). The E metrics defining the average peak-to-valley ratio are $2.98^{+0.60}_{-0.47}$, $2.14^{+0.26}_{-0.21}$, and $6.05^{+3.87}_{-2.14}$ respectively.

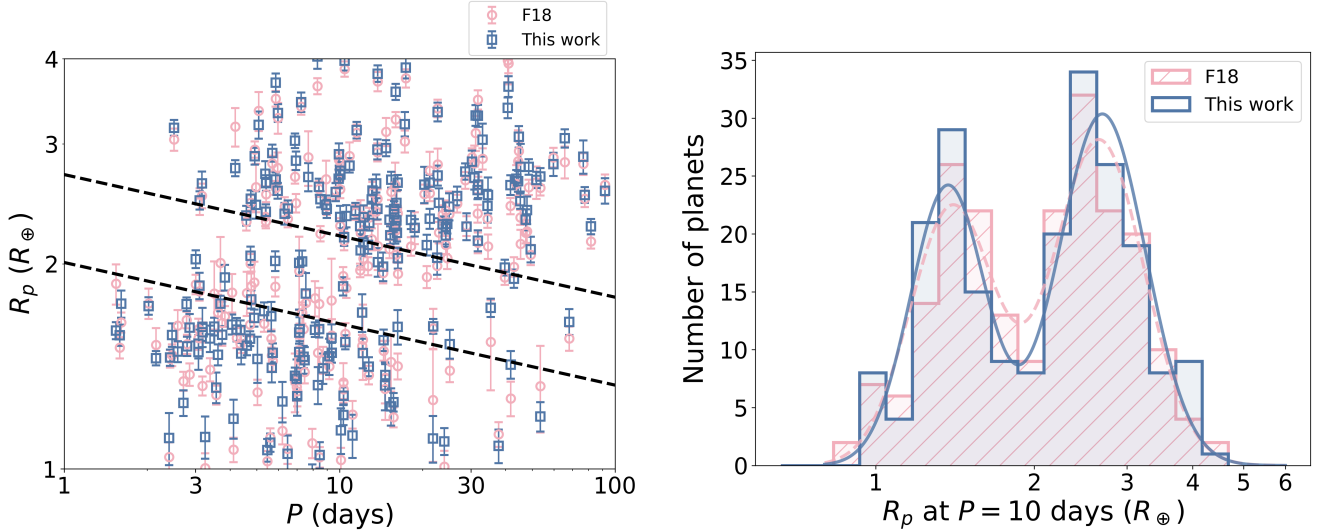


Figure 15. Left: Radius-period plot of the 211 planets common to this work (blue) and F18 (red), using the same stellar radii to calculate planetary radii. Right: Same as Figure 14, but the planetary population is filtered to the 211 common planets in both samples. Planets in both samples are adjusted to equivalent radii at $P = 10$ days according to the slope calculated in Section 3.2 with the SVM. The red and blue histograms are produced with the parameters obtained from F18 and this work respectively. The histograms and fitting with the Gaussian Mixture Model show that the observed valley is deeper in this work.

Mullally et al. (2015) assumed a circular orbit when performing the transit fits. On the contrary, we leave orbital eccentricity e as a free parameter, and place a prior on e based on the expected distribution from Van Eylen et al. (2019) and the stellar density ρ_* from F18. However, most of the planets in our sample have near-circular orbits, with over 85% of planets having $e < 0.1$. Therefore planetary orbital eccentricity is not sufficient to explain the difference between the two results. The possible presence of TTVs also do not contribute to the discrepancy as planets with known TTVs are excluded in our like-for-like planet comparisons. In fact, when fitting transits using identical methods, precisions in R_p/R_* obtained from fitting transit light curves of shorter cadences has been found to substantially improve, compared to 30-minute cadence light curves (Camero, Ho & Van Eylen, in prep.). We therefore expect the photometry cadence to

contribute significantly to the difference in the views of the radius valley. Further work, such as refitting the long cadence data of the same planet population with identical transit fitting methods, is needed to further investigate the effect of light curve cadence on planet parameter estimates and the radius valley. We leave such considerations for future studies.

4.4 Radius valley relation with stellar age consistent with core-powered mass loss model

In Section 3.5, we present a positive relationship between the radius valley location and stellar age. Photoevaporation is predicted to occur in the first 100 Myr of the planet's formation (Owen & Wu 2017), well before observations are able to detect the evolution signals, whereas

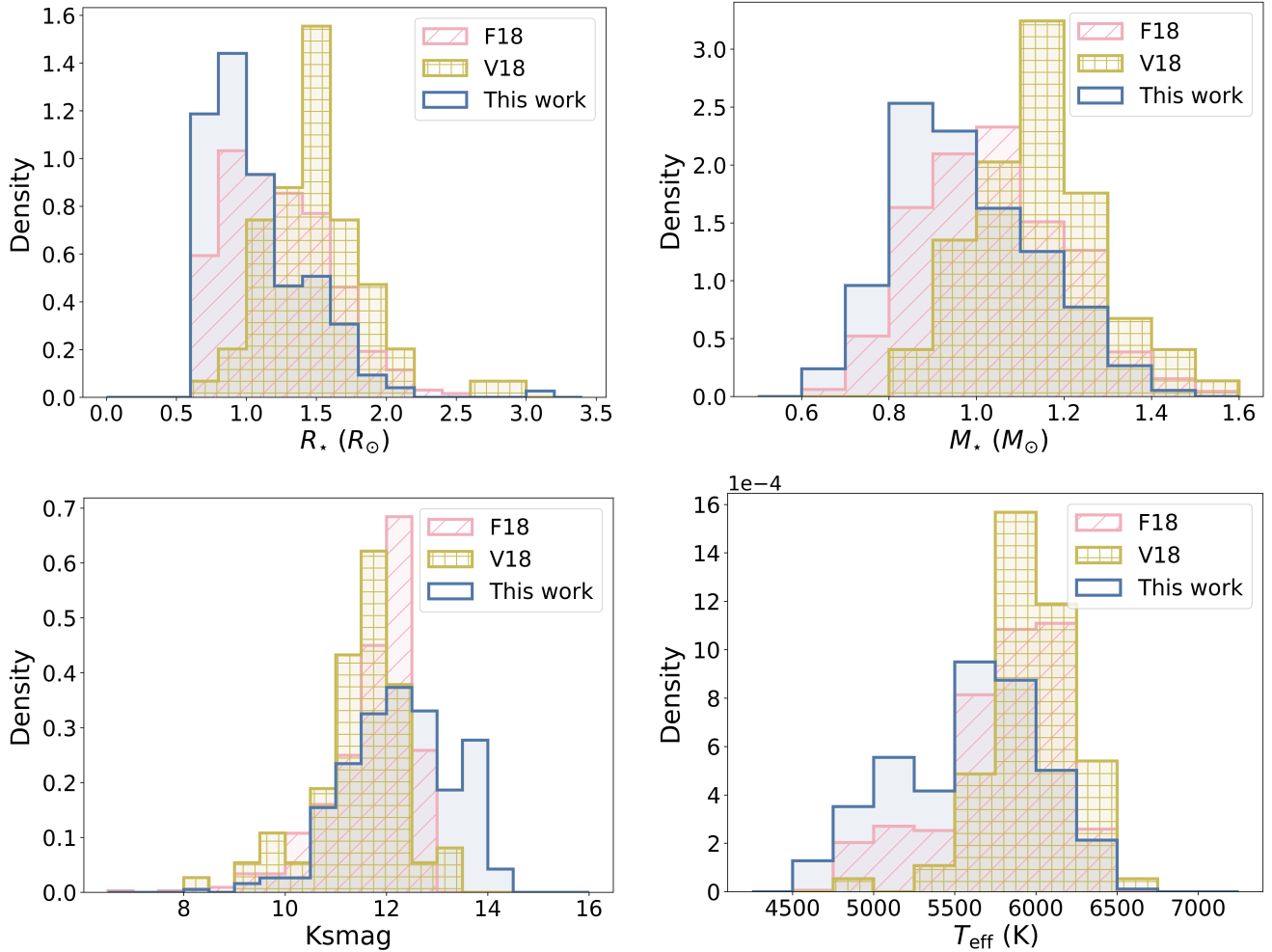


Figure 16. Distribution of host stars parameters in our work, compared with F18 and V18. The properties shown here, from top left to bottom right, are stellar radius R_* , mass M_* , *Kepler* magnitude Ksmag, and effective temperature T_{eff} . For systems with multiple transiting planets, stars are counted multiple times.

Table 9. Average values of stellar properties of the host stars in the planetary sample used in this work, compared with F18 and V18. \bar{x} and \tilde{x} represent the mean and median values of the parameter x respectively.

Sample	\bar{R}_* (R_\odot)	\tilde{R}_* (R_\odot)	\bar{M}_* (M_\odot)	\tilde{M}_* (M_\odot)	Ks $\bar{\text{mag}}$	Ks $\tilde{\text{mag}}$	$T_{\text{eff}}^{\bar{}}$ (K)	$T_{\text{eff}}^{\tilde{}}$ (K)
This work	1.08	0.99	0.98	0.95	12.27	12.31	5587	5630
F18	1.23	1.19	1.04	1.03	11.72	11.97	5788	5860
V18	1.50	1.45	1.14	1.14	11.49	11.57	5980	5952

core-powered mass loss occurs throughout the main-sequence lifetime of the stars, on Gyr timescales (Ginzburg et al. 2016; Gupta & Schlichting 2019, 2020). Hence, in the photoevaporation case, the radius valley is expected to be located at a constant radius. On the other hand, in the core-powered mass loss case, the radius valley shifts to higher planet radii for older systems, as the atmospheres of planets with more massive cores are stripped off later in the evolution process than their less massive counterparts (e.g. David et al. 2021; Rogers & Owen 2021).

Our results reveal a weak positive radius valley dependence on the stellar age, which is consistent with the core-powered mass loss scenario, as is the observed radius valley dependence on stellar mass as discussed in Section 4.2. However, a small age dependence does not preclude photoevaporation, since even in this scenario a subset of planets may still lose their atmospheres and evolve at Gyr timescales

(David et al. 2021; Rogers et al. 2021), and we are unable to observe stars younger than 100 Myr and hence cannot rule out the possibility of a dominant photoevaporation effect on planets at the early stages of the stars' lifetime. Also, stellar age measurements are highly uncertain; the mean percentage uncertainty in stellar age for our sample is 54%, hence there is also a probability that some stars are younger than observed.

Table 10 lists the 50 planets located inside the radius valley in our sample. To do so, we here defined the new radius valley region as the area bounded by the two lines passing through the supporting vectors in the 4D SVM model in Section 3.5, given by equation 15 with $A = -0.096$, $B = 0.231$, $C = 0.033$, $D_{\text{lower}} = 0.272$ for the lower line, and $D_{\text{upper}} = 0.405$ for the upper line. These planets are potentially interesting for future characterisation study as their

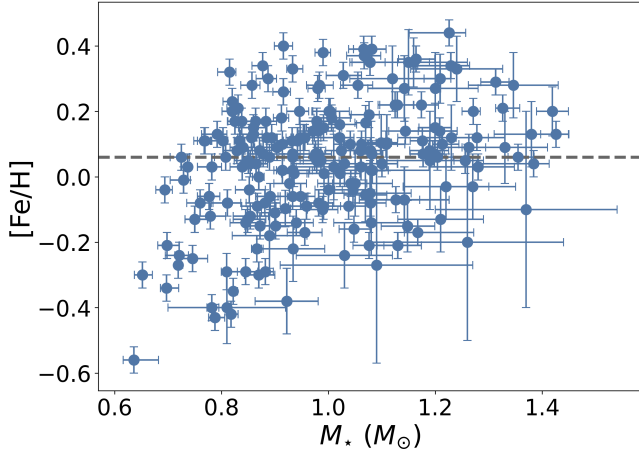


Figure 17. Metallicity and mass of the host stars used in this work. The grey dotted line $[\text{Fe}/\text{H}] = 0.06$ shows the cut-off between stars of low and high metallicity as defined in this work. We note a lack of stars with low metallicity and large stellar mass.

atmospheres and interiors may provide additional insights regarding formation and evolution mechanisms.

4.5 Radius valley depth varies with stellar metallicity

In Section 3.6, we show a higher average E value (i.e. a deeper radius valley) for planets around metal-poor stars. This seems to contradict the suggestion that the radius valley is deeper for planets around metal-rich stars (Owen & Murray-Clay 2018). However, we note from Figure 17, that in our sample, the metal-rich host stars span a wider range of stellar masses, due to lack of metal-poor stars with large radii. As from Section 3.4 we observe that the radius valley depends on stellar mass as well, the superposition of the radius valley for different stellar masses potentially smears the gap, making the radius valley appear shallower.

The degeneracy between stellar mass and metallicity is not fully resolved, hence we are unable to determine the sole effect of stellar metallicity on the radius valley in this work. We therefore consider the results related to metallicity to be inconclusive and in need of further future study.

5 CONCLUSION

In summary, we performed transit light curve fitting on 431 planets using *Kepler* 1-minute short cadence data, the vast majority of which have not been previously analysed homogeneously using short cadence observations. In this paper, we presented their revised planetary parameters, which in some cases differ substantially from those previously reported. These differences are unrelated to stellar parameters but may be related to the details of the transit fitting approach or the shorter observing cadence, the effects of which should be disentangled in future studies.

By statistically analysing the small close-in planets in our sample, we observed a radius valley which is deeper than that reported in several other studies, although not entirely empty. The valley’s depth likely implies a homogeneous initial planetary core composition where the planets are similar in composition at formation, and

likely to have similar iron fractions. We provide a table of those planets that appear to be inside the valley, as they may warrant further study.

The radius valley has a strong dependence on planetary orbital period and the mass of the host star. It also displays a weak dependence on the stellar age. We compared several possible radius valley models using support vector machines. We determined that the radius valley can best be described in four dimensions using the formula

$$R_{p,\text{valley}} \propto P^A M_{\star}^B (\text{age})^C \quad (20)$$

with $A = -0.096^{+0.023}_{-0.027}$, $B = 0.231^{+0.053}_{-0.064}$, and $C = 0.033^{+0.017}_{-0.025}$.

Comparing our radius valley dependencies with theoretical models, we found that in R_p - S - M_{\star} space, our posterior distributions are most consistent with core-powered mass loss, where they agree within less than 1σ . The models are also consistent with photoevaporation scenarios at $\approx 2\sigma$. We did not find a significant dependence of the radius valley on stellar metallicity.

With the Transiting Exoplanet Survey Satellite (TESS, e.g. Ricker et al. 2015) now in its extended mission, and the upcoming launch of the PLANetary Transits and Oscillations of stars (PLATO) mission (e.g. Rauer et al. 2014), such future planetary studies could drastically increase the number of planets with radii measurements and hence provide an even more detailed view of the radius valley. This work highlights the impact of careful transit fitting using short, 1-minute cadence observations to obtain precise planetary radii. This will likely be of key importance to derive precise planetary radii using transit observations from ongoing and future missions, which will ultimately allow us to better understand the formation and evolution of small close-in planets.

ACKNOWLEDGEMENTS

C.S.K.H. would like to thank the Science and Technology Facilities Council (STFC) for funding support through a PhD studentship. We would like to thank Erik Petigura, James Rogers, and James Owen for insightful discussions. We also thank the anonymous reviewer for taking their time to review the paper, and for their valuable suggestions which have improved the manuscript.

DATA AVAILABILITY

The *Kepler* 1-minute short cadence light curves are available for download on the NASA Mikulski Archive for Space Telescopes (MAST) database¹. The parameter estimates from HMC posteriors are provided in the Appendix tables.

REFERENCES

- Astropy Collaboration et al., 2013, *A&A*, **558**, A33
- Astropy Collaboration et al., 2018, *AJ*, **156**, 123
- Berger T. A., Huber D., Gaidos E., van Saders J. L., Weiss L. M., 2020, *AJ*, **160**, 108
- Bourque M., et al., 2021, The Exoplanet Characterization Toolkit (ExoCTK), doi:10.5281/zenodo.4556063, <https://doi.org/10.5281/zenodo.4556063>
- Claret A., Bloemen S., 2011, *A&A*, **529**, A75
- Cloutier R., Menou K., 2020, *AJ*, **159**, 211
- David T. J., et al., 2021, *AJ*, **161**, 265

¹ <https://archive.stsci.edu>

Table 10. List of planets inside the radius valley as defined by this work. The coordinates (RA and Dec) are taken from *Kepler* Q1-17 Data Release 25 catalogue (Thompson et al. 2018), except for K02533.03, where data is taken from *Kepler* Q1-16 catalogue (Mullally et al. 2015).

KOI	Kepler name	P (days)	t_0 (BJD-2454833)	R_p/R_\star	$R_p (R_\oplus)$	RA (deg)	Dec (deg)
K00049.01	Kepler-461 b	8.313784 ± 0.000015	175.9915 ± 0.0008	0.0287 ± 0.0010	$4.03^{+0.17}_{-0.17}$	292.24902	46.164822
K00070.03	Kepler-20 A d	77.611598 ± 0.000019	164.7274 ± 0.0005	0.0263 ± 0.0003	$2.52^{+0.07}_{-0.07}$	287.698	42.338718
K00092.01	KOI-92.01	65.704594 ± 0.000018	137.4419 ± 0.0005	0.0263 ± 0.0006	$3.02^{+0.11}_{-0.11}$	283.37482	43.788219
K00094.02	Kepler-89 A c	10.423684 ± 0.000005	138.0092 ± 0.0005	0.0266 ± 0.0006	$3.97^{+0.13}_{-0.13}$	297.33307	41.891121
K00105.01	Kepler-463 b	8.981015 ± 0.000002	136.6493 ± 0.0005	0.0313 ± 0.0004	$3.65^{+0.11}_{-0.10}$	298.93704	44.85791
K00107.01	Kepler-464 b	7.256964 ± 0.000011	134.0232 ± 0.0007	0.0198 ± 0.0004	$3.46^{+0.11}_{-0.11}$	294.83517	48.982361
K00108.01	Kepler-103 b	15.965333 ± 0.000013	142.1780 ± 0.0006	0.0221 ± 0.0002	$3.49^{+0.04}_{-0.04}$	288.98456	40.064529
K00111.03	Kepler-104 A d	51.755294 ± 0.000018	271.0894 ± 0.0005	0.0232 ± 0.0003	$2.66^{+0.07}_{-0.07}$	287.60461	42.166779
K00122.01	Kepler-95 b	11.523073 ± 0.000005	131.9686 ± 0.0004	0.0205 ± 0.0002	$3.24^{+0.10}_{-0.10}$	284.48245	44.398041
K00157.02	Kepler-11 d	22.687159 ± 0.000014	148.4549 ± 0.0006	0.0282 ± 0.0006	$3.34^{+0.11}_{-0.10}$	297.11511	41.909142
K00174.01	Kepler-482 b	56.354185 ± 0.000019	144.8366 ± 0.0007	0.0339 ± 0.0013	$2.92^{+0.14}_{-0.14}$	296.82291	48.107552
K00238.01	Kepler-123 b	17.232309 ± 0.000018	135.0923 ± 0.0008	0.0223 ± 0.0006	$3.21^{+0.13}_{-0.13}$	296.99863	42.78196
K00285.01	Kepler-92 b	13.748833 ± 0.000015	179.2788 ± 0.0007	0.0198 ± 0.0003	$3.71^{+0.06}_{-0.06}$	289.08606	41.562958
K00317.01	Kepler-521 b	22.208119 ± 0.000015	206.3592 ± 0.0006	0.0207 ± 0.0003	$3.69^{+0.11}_{-0.11}$	298.81638	43.998039
K00351.03	Kepler-90 d	59.737034 ± 0.000020	158.9612 ± 0.0009	0.0217 ± 0.0006	$2.80^{+0.11}_{-0.11}$	284.4335	49.305161
K00351.04	Kepler-90 e	91.940461 ± 0.000020	134.2987 ± 0.0010	0.0198 ± 0.0007	$2.56^{+0.11}_{-0.11}$	284.4335	49.305161
K00386.01	Kepler-146 b	31.158789 ± 0.000019	173.9038 ± 0.0009	0.0297 ± 0.0007	$3.30^{+0.12}_{-0.12}$	294.11075	38.710232
K00386.02	Kepler-146 c	76.732517 ± 0.000020	200.6716 ± 0.0010	0.0258 ± 0.0013	$2.87^{+0.16}_{-0.16}$	294.11075	38.710232
K00408.01	Kepler-150 c	7.381981 ± 0.000007	173.0729 ± 0.0008	0.0355 ± 0.0005	$3.34^{+0.12}_{-0.12}$	288.2341	40.520901
K00416.01	Kepler-152 b	18.207957 ± 0.000015	185.8427 ± 0.0006	0.0383 ± 0.0006	$3.12^{+0.10}_{-0.09}$	286.86548	41.989079
K00435.05	Kepler-154 c	62.302788 ± 0.000020	179.0982 ± 0.0010	0.0266 ± 0.0010	$3.04^{+0.15}_{-0.15}$	289.78052	49.89653
K00509.02	Kepler-171 c	11.463477 ± 0.000013	137.3859 ± 0.0008	0.0328 ± 0.0008	$3.30^{+0.15}_{-0.14}$	296.77191	41.755539
K00510.04	Kepler-172 e	35.118523 ± 0.000020	152.1229 ± 0.0010	0.0248 ± 0.0021	$2.82^{+0.26}_{-0.26}$	283.36841	41.821861
K00555.02	Kepler-598 c	86.494779 ± 0.000020	181.8831 ± 0.0009	0.0272 ± 0.0008	$2.51^{+0.10}_{-0.10}$	293.12341	40.934769
K00665.01	Kepler-207 d	5.868083 ± 0.000009	170.3244 ± 0.0009	0.0202 ± 0.0004	$3.69^{+0.11}_{-0.11}$	290.03052	42.16605
K00707.02	Kepler-33 f	41.028059 ± 0.000019	172.5788 ± 0.0009	0.0207 ± 0.0004	$3.64^{+0.13}_{-0.13}$	289.07755	46.005219
K00707.03	Kepler-33 e	31.784774 ± 0.000020	135.8721 ± 0.0009	0.0188 ± 0.0005	$3.30^{+0.12}_{-0.12}$	289.07755	46.005219
K00708.01	Kepler-216 c	17.406653 ± 0.000017	171.0063 ± 0.0008	0.0230 ± 0.0006	$3.88^{+0.14}_{-0.14}$	293.72806	46.12915
K00711.01	Kepler-218 c	44.699505 ± 0.000020	174.8232 ± 0.0008	0.0272 ± 0.0007	$3.07^{+0.11}_{-0.11}$	295.41281	46.266472
K00800.02	Kepler-234 c	7.212030 ± 0.000017	172.8172 ± 0.0009	0.0283 ± 0.0012	$3.61^{+0.28}_{-0.26}$	291.65353	38.494659
K00834.02	Kepler-238 d	13.233546 ± 0.000019	140.3211 ± 0.0010	0.0197 ± 0.0005	$3.37^{+0.19}_{-0.18}$	287.89713	40.637821
K00834.05	Kepler-238 f	50.447315 ± 0.000020	178.4929 ± 0.0010	0.0203 ± 0.0009	$3.48^{+0.23}_{-0.22}$	287.89713	40.637821
K00881.01	Kepler-712 b	21.022471 ± 0.000017	207.6765 ± 0.0007	0.0391 ± 0.0008	$3.14^{+0.18}_{-0.17}$	294.90973	42.935261
K00907.04	Kepler-251 e	99.640965 ± 0.000021	198.6899 ± 0.0009	0.0320 ± 0.0017	$2.82^{+0.19}_{-0.19}$	296.56622	44.105862
K00921.02	Kepler-253 d	18.119898 ± 0.000018	182.6165 ± 0.0008	0.0346 ± 0.0011	$3.01^{+0.16}_{-0.15}$	291.84198	44.858089
K00934.01	Kepler-254 b	5.826654 ± 0.000006	173.0110 ± 0.0009	0.0368 ± 0.0011	$3.62^{+0.26}_{-0.24}$	288.1647	45.816509
K00941.01	Kepler-257 c	6.581482 ± 0.000009	174.7876 ± 0.0009	0.0429 ± 0.0009	$3.75^{+0.15}_{-0.15}$	297.31598	46.023258
K00954.02	Kepler-259 c	36.924954 ± 0.000019	174.2245 ± 0.0010	0.0291 ± 0.0017	$2.85^{+0.19}_{-0.19}$	288.21194	46.615002
K01001.01	Kepler-264 b	40.806846 ± 0.000020	155.7126 ± 0.0009	0.0159 ± 0.0003	$3.30^{+0.12}_{-0.12}$	292.04462	37.37624
K01198.01	Kepler-275 c	16.088329 ± 0.000018	139.4928 ± 0.0010	0.0232 ± 0.0011	$3.55^{+0.31}_{-0.29}$	292.47971	38.514919
K01215.02	Kepler-277 c	33.006310 ± 0.000020	145.3914 ± 0.0010	0.0161 ± 0.0008	$3.04^{+0.17}_{-0.17}$	286.58316	39.077202
K01270.01	Kepler-57 b	5.729326 ± 0.000005	138.5598 ± 0.0009	0.0356 ± 0.0024	$3.16^{+0.24}_{-0.24}$	293.6413	44.65704
K01486.02	Kepler-302 b	30.183689 ± 0.000018	146.6480 ± 0.0009	0.0286 ± 0.0011	$3.27^{+0.21}_{-0.20}$	294.31699	43.629341
K01563.04	Kepler-305 d	16.738655 ± 0.000019	359.4178 ± 0.0009	0.0338 ± 0.0022	$2.84^{+0.22}_{-0.22}$	299.22433	40.343182
K01598.01	Kepler-310 c	56.476167 ± 0.000019	143.8052 ± 0.0008	0.0301 ± 0.0007	$2.75^{+0.10}_{-0.10}$	288.83936	46.98674
K02051.01	Kepler-355 c	25.762459 ± 0.000020	147.7050 ± 0.0009	0.0230 ± 0.0010	$2.95^{+0.18}_{-0.17}$	285.79947	42.811779
K02390.01	Kepler-1219 b	16.104672 ± 0.000020	135.0156 ± 0.0010	0.0120 ± 0.0011	$3.51^{+0.46}_{-0.46}$	297.21579	47.378521
K02414.02	Kepler-384 c	45.348527 ± 0.000020	142.2527 ± 0.0010	0.0157 ± 0.0012	$2.78^{+0.22}_{-0.22}$	286.02612	44.782871
K02533.03	KOI-2533.03	26.115290 ± 0.000019	145.5642 ± 0.0010	0.0122 ± 0.0011	$4.01^{+0.38}_{-0.38}$	286.71564	48.645279
K02639.01	KOI-2639.01	25.108060 ± 0.000020	146.4407 ± 0.0010	0.0191 ± 0.0083	$3.69^{+1.63}_{-1.62}$	285.36517	49.201561

- Foreman-Mackey D., et al., 2021, *The Journal of Open Source Software*, 6, 3285
- Fulton B. J., Petigura E. A., 2018, *AJ*, 156, 264
- Fulton B. J., et al., 2017, *AJ*, 154, 109
- Furlan E., et al., 2017, *AJ*, 153, 71
- Ginsburg A., et al., 2019, *AJ*, 157, 98
- Ginzburg S., Schlichting H. E., Sari R., 2016, *ApJ*, 825, 29
- Ginzburg S., Schlichting H. E., Sari R., 2018, *MNRAS*, 476, 759
- Gupta A., Schlichting H. E., 2019, *MNRAS*, 487, 24
- Gupta A., Schlichting H. E., 2020, *MNRAS*, 493, 792
- Holczer T., et al., 2016, *ApJS*, 225, 9
- Huber D., et al., 2013, *ApJ*, 767, 127
- Kipping D. M., 2013, *MNRAS*, 435, 2152
- Lee E. J., Chiang E., 2016, *ApJ*, 817, 90
- Lee E. J., Chiang E., Ormel C. W., 2014, *ApJ*, 797, 95
- Lightkurve Collaboration et al., 2018, Lightkurve: Kepler and TESS time series analysis in Python, Astrophysics Source Code Library (ascl:1812.013)
- Lopez E. D., Fortney J. J., 2013, *ApJ*, 776, 2
- Lopez E. D., Rice K., 2018, *MNRAS*, 479, 5303
- Lloyd R. O. P., Shkolnik E. L., Schneider A. C., Richey-Yowell T., Barman T. S., Peacock S., Pagano I., 2020, *ApJ*, 890, 23
- Lundkvist M. S., et al., 2016, *Nature Communications*, 7, 11201
- Luque R., Pallé E., 2022, *Science*, 377, 1211
- MacDonald M. G., 2019, *MNRAS*, 487, 5062
- Martinez C. F., Cunha K., Ghezzi L., Smith V. V., 2019, *ApJ*, 875, 29
- Mathur S., et al., 2017, *ApJS*, 229, 30
- Mordasini C., 2020, *A&A*, 638, A52
- Mullally F., et al., 2015, *ApJS*, 217, 31
- Owen J. E., Adams F. C., 2019, *MNRAS*, 490, 15
- Owen J. E., Murray-Clay R., 2018, *MNRAS*, 480, 2206
- Owen J. E., Wu Y., 2013, *ApJ*, 775, 105
- Owen J. E., Wu Y., 2017, *ApJ*, 847, 29
- Petigura E. A., 2020, *AJ*, 160, 89
- Petigura E. A., et al., 2017, *AJ*, 154, 107
- Petigura E. A., et al., 2022, *AJ*, 163, 179
- Raghavan D., et al., 2010, *ApJS*, 190, 1
- Rasmussen C. E., Williams C. K. I., 2006, *Gaussian Processes for Machine Learning*. The MIT Press
- Rauer H., et al., 2014, *Experimental Astronomy*, 38, 249
- Ricker G. R., et al., 2015, *Journal of Astronomical Telescopes, Instruments, and Systems*, 1, 014003
- Rogers J. G., Owen J. E., 2021, *MNRAS*, 503, 1526
- Rogers J. G., Gupta A., Owen J. E., Schlichting H. E., 2021, *MNRAS*, 508, 5886
- Rowe J. F., et al., 2014, *ApJ*, 784, 45
- Salvatier J., Wiecki T. V., Fonnesbeck C., 2016, *PeerJ Computer Science*, 2, e55
- Silva Aguirre V., et al., 2015, *MNRAS*, 452, 2127
- Smith J. C., et al., 2012, *PASP*, 124, 1000
- Stumpe M. C., et al., 2012, *PASP*, 124, 985
- Thompson S. E., et al., 2018, *ApJS*, 235, 38
- Van Eylen V., Albrecht S., 2015, *ApJ*, 808, 126
- Van Eylen V., Agentoft C., Lundkvist M. S., Kjeldsen H., Owen J. E., Fulton B. J., Petigura E., Snellen I., 2018, *MNRAS*, 479, 4786
- Van Eylen V., et al., 2019, *AJ*, 157, 61
- Van Eylen V., et al., 2021, *MNRAS*, 507, 2154

APPENDIX A: EXTRA MATERIAL

Table A3. Transit jitter and GP parameters from transit fitting of planetary systems in this work. Only the first 10 systems are shown here; the full table is available online in a machine-readable format.

KOI	$\log \sigma_{\text{lc}}$	$\log \sigma_{\text{gp}}$	$\log \rho_{\text{gp}}$
41	-8.4379 ± 0.0016	-9.5822 ± 0.0105	-4.5121 ± 0.0335
46	-7.1119 ± 0.0037	-9.1794 ± 0.1025	-4.3449 ± 0.2492
49	-7.3268 ± 0.0044	-8.8595 ± 0.0680	-1.2568 ± 0.1547
69	-8.9861 ± 0.0019	-10.1248 ± 0.0133	-4.8968 ± 0.0382
70	-7.7689 ± 0.0012	-9.4665 ± 0.0150	-3.7110 ± 0.0415
72	-8.4175 ± 0.0053	-9.6473 ± 0.0392	-4.0440 ± 0.1139
82	-8.1671 ± 0.0018	-8.6193 ± 0.0116	-3.2278 ± 0.0240
85	0.0000 ± 0.0000	0.0000 ± 0.0000	0.0000 ± 0.0000
92	-8.1505 ± 0.0062	-9.8036 ± 0.0880	-3.9919 ± 0.2448
94	-7.8819 ± 0.0017	-9.8028 ± 0.0308	-2.9898 ± 0.1183
...

This paper has been typeset from a $\text{\TeX}/\text{\LaTeX}$ file prepared by the author.